

ADA037245

Final
AFOSR Interim Report - Part I

12

CHARGED PARTICLE LABORATORY REPORT NO. 2-76

DESIGN AND CONSTRUCTION
OF A DENSE PLASMA FOCUS DEVICE

BY

DAVID LEE WILLENBORG
CHARLES D. HENDRICKS

CHARGED PARTICLE RESEARCH LABORATORY
DEPARTMENT OF ELECTRICAL ENGINEERING
UNIVERSITY OF ILLINOIS
URBANA, ILLINOIS 61801

Contract No. AFOSR-74-2643
Project Task No. 9751-03



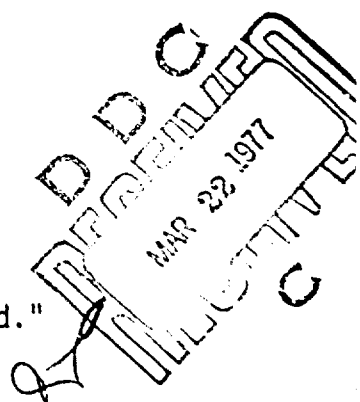
October 1976

Distribution Statement

"Approved for public release; distribution unlimited."

Research Sponsored By

THE AIR FORCE OFFICE OF SCIENTIFIC RESEARCH
OFFICE OF AEROSPACE RESEARCH
UNITED STATES AIR FORCE



Reproduction, translation, publication, use and
disposal in whole or in part by or for the
United States Government is permitted.

AIR FORCE OFFICE OF SCIENTIFIC RESEARCH (AFSC)
NOTICE OF TRANSMITTAL TO DDC
This technical report has been reviewed and is
approved for public release IAW AFR 190-12 (7b).
Distribution is unlimited.

A. D. BLOSE
Technical Information Officer

UNCLASSIFIED

SECURITY CLASSIFICATION OF THIS PAGE (When Data Entered)

REPORT DOCUMENTATION PAGE		READ INSTRUCTIONS BEFORE COMPLETING FORM
1. REPORT NUMBER 18 AFOSR - TR - 77 - 0184	2. GOVT ACCESSION NO.	3. PECI-ENT'S CATALOG NUMBER
4. TITLE (and subtitle) DESIGN AND CONSTRUCTION OF A DENSE PLASMA FOCUS DEVICE.	5. PERIOD OF REPORT & PERIOD COVERED FINAL REPORT, (PART 1),	
6. AUTHOR(s) David Lee Willenborg Charles D. Hendricks	7. 14 15 ✓ AF	8. PERIODICITY & REPORT NUMBER CPRI-2-76, OTLU-FMG-76-2557 CONTRACT OR GRANT NUMBER AFOSR 77-2643-384
9. PERFORMING ORGANIZATION NAME AND ADDRESS University of Illinois-Dept. of Electrical Eng. Charged Particle Laboratory Urbana, Illinois	10. PROGRAM ELEMENT, PROJECT, TASK & WORK UNIT NUMBERS 9751-103 611102F	
11. CONTROLLING OFFICE NAME AND ADDRESS AF Office of Scientific Research /NP Bolling AFB DC 20332	12. REPORT DATE Oct 1976	
13. MONITORING AGENCY NAME & ADDRESS (if different from Controlling Office)	14. NUMBER OF PAGES 93	
	15. SECURITY CLASSIFICATION (of this report) UNCLASSIFIED	
	15a. DECLASSIFICATION/DOWNGRADING SCHEDULE	
16. DISTRIBUTION STATEMENT (of this Report) Approved for public release; distribution unlimited.		
17. DISTRIBUTION STATEMENT (of the abstract entered in Block 20, if different from Report)		
18. SUPPLEMENTARY NOTES		
19. KEY WORDS (Continue on reverse side if necessary and identify by block number) Dense Plasma Focus Dense Plasma Focus Circuit Pulse Circuit Pulsed X-ray Generation Instrumentation		
20. ABSTRACT (Continue on reverse side if necessary and identify by block number) This paper deals with the design of a dense plasma focus device as an engineering project. Essentially this approach can be summarized as follows: First, an introduction dealing with a general discussion of plasma devices focusing on the role of a dense plasma focus device as a useful tool in future research; second, an explanation of the operation of the dense plasma focus; third, a general design discussion of the dense plasma focus device; fourth, specification next of a realizable system; and finally, a discussion of the problems encountered in (over)		

UNCLASSIFIED

cont

SECURITY CLASSIFICATION OF THIS PAGE (When Data Entered)

20. → constructing this design and observations concerning the effectiveness of this dense plasma focus design. ↑

DESIGN AND CONSTRUCTION
OF A DENSE PLASMA FOCUS DEVICE

Final
Interim Report - Part I

October 1976

Contract No. AFOSR-74-2643
Project Task No. 9751-03

Submitted by

David Lee Willenborg
Charles D. Hendricks
Charged Particle Laboratory
University of Illinois
Urbana, Illinois

ACCESSION NO.	
NTIS	White Section
300	Buff Section <input type="checkbox"/>
TELETYPE	
JOURNAL	
JUSTIFICATION	
BY	
DISTRIBUTION/AVAILABILITY CODES	
Dist.	AVAIL. FOR SPECIAL
<input checked="" type="checkbox"/>	

ABSTRACT

This paper deals with the design of a dense plasma focus device as an engineering project. Essentially this approach can be summarized as follows: First, an introduction dealing with a general discussion of plasma devices focusing on the role of a dense plasma focus device as a useful tool in future research; second, an explanation of the operation of the dense plasma focus; third, a general design discussion of the dense plasma focus device; fourth, specification of a realizable system; and finally, a discussion of the problems encountered in constructing this design and observations concerning the effectiveness of this dense plasma focus design.

ACKNOWLEDGMENT

The research for this report was supported by the United States Air Force Office of Scientific Research Grant AFOSR-74-2643.

TABLE OF CONTENTS

	Page
1. INTRODUCTION	1
2. THEORETICAL DEVICE OPERATION	3
2.1 Breakdown Phase	5
2.2 The Acceleration Phase.	8
2.3 Collapse Phase.	12
3. DENSE PLASMA FOCUS DEVICE DESIGN	21
3.1 Mather- vs. Filipov-Type Device	21
3.2 Dense Plasma Focus Device Configuration	23
3.3 Detailed Dense Plasma Focus Device Design	25
3.3.1 The inner electrode design	27
3.3.2 The outer electrode design	29
3.3.3 End-plate spacer design.	31
3.3.4 The electrode insulator design	32
3.3.5 Other device design considerations	34
4. EXPERIMENTAL SYSTEM.	36
4.1 Energy Storage and Transmission	36
4.2 Fast High-Energy Switch	42
4.2.1 Tube-type and mechanical switches.	42
4.2.2 Electrical discharge initiated switches.	43
4.2.2.1 Vacuum spark gaps	43
4.2.2.2 Solid dielectric spark gap.	45
4.2.2.3 Gas dielectric spark gaps	48
4.2.3 System switch design	51
4.2.4 System switch trigger.	55
4.3 Vacuum and Gas Control System	60
4.4 Device Diagnostics.	62
4.4.1 Electrical instrumentation	63
4.4.1.1 Voltage measurement device.	64
4.4.1.2 Current measurement device.	68
4.4.2 X-ray measurements	73
4.5 Shielding and Grounding	74
4.6 High-Voltage Charging System.	78
5. DEVICE OPERATION	82

	Page
6. SUMMARY	84
REFERENCES	85

LIST OF FIGURES

Figure	Page
1. Typical dense plasma focus apparatus	4
2. Dense plasma focus device breakdown phase.	6
3. Typical device waveforms	11
4. Fluid models of pinch mechanisms	16
5. Ion trajectory models.	19
6. Fillipov-type plasma focus device.	22
7. Various device geometries.	24
8. Experimental dense plasma focus device	26
9. Dense plasma focus experimental system	37
10a. The capacitor bank arrangement	38
10b. Equivalent electrical circuit of bank and gun.	38
11. Solid dielectric switch types.	47
12. Gas dielectric switch types.	50
13a. The front view of the spark gap.	52
13b. The side view of the spark gap	52
14a. Pulse amplifier.	56
14b. Triggering circuit for the thyratron tube and spark gap.	57
15. Vacuum system.	61
16a. Coaxial capacitative high-voltage divider.	65
16b. Capacitative divider circuit	67
17a. Rogowski loop circuit.	70
17b. Rogowski loop current probe.	72
18. Solid-state x-ray detector circuit	75
19. High-voltage system.	80
20. High-voltage control sensing circuit	81

1. INTRODUCTION

Most of the universe, with a few exceptions like the earth, is composed of gaseous plasma in various densities. In addition to naturally occurring plasma, man has succeeded in producing artificial plasma for his own personal use, with nuclear fusion probably the most exciting and socially constructive application. Nuclear fusion has the potential to supply the world with abundant, inexpensive, environmentally clean energy for hundreds of years.

Fundamentally, the fusion problem is one of bringing the reacting particles close enough together for sufficient time to allow fusion to occur. The particles, which must approach to within atomic radii distances, require kinetic energies of around 10^5 eV to overcome the large repulsive Coulomb forces between nuclei. A practical figure of merit for fusion reaction is Lawson's Criterion [1] which is: $n\tau = 10^{14}$, where n = plasma density in cm^{-3} , and τ = containment time in seconds at a plasma temperature of 10^5 eV. Achieving temperatures of 10^5 eV is technically feasible but maintaining a dense enough plasma for sufficient time is pushing technology to the limit. At present, neither laser fusion nor magnetic confinement schemes have come close to Lawson's Criterion; however, plasma pinch devices have come very close, with the dense plasma focus device one of the most promising.

The dense plasma focus is a form of electromagnetic shock tube that causes rapid compression and heating of the plasma during a fast coaxial pinch called a focus. The gas in a plasma focus may reach densities of 10^{19} to 10^{20} cm^{-3} and temperatures of a few keV during the several hundred nanosecond long pinch. The device characteristics produce a plasma near Lawson's Criterion, but it is important to note that the focus mechanism

is not well-understood and that the scaling laws are not well-defined. Thus, to consider the dense plasma focus device as a fusion generator, a more complete understanding of the device is necessary. The dense plasma focus is presently a valuable tool in the study of dense plasma interactions and a source of high-energy x-ray pulses and neutron pulses on the order of 10^{12} neutrons per shot despite the lack of understanding of device operation.

The dense plasma focus was discovered independently by Fillipov et al. [4], [5] in the early 1960's and shortly after by Mather [2], [3], who used a coaxial gun geometry. Since then several variations of these two original designs have been constructed in more than seventeen laboratories in at least six countries. The interest in this device is great and for obvious reasons. The device discussed in this paper was primarily constructed to study x-ray generation and possible enhancement. This paper will deal with the design, construction and operation of this device with emphasis on experimental technique.

2. THEORETICAL DEVICE OPERATION

The dense plasma focus effect has been studied extensively in recent years, yet the mechanism producing the dense, relatively long-lived plasma focus remains a mystery. The device appears simple to construct, but as the discussion in Section 3.3 will reveal, there are certain design parameters that must be carefully considered for the production of a plasma pinch. Essentially, the device, referred to as a gun in dense plasma focus literature, consists of a center metal cylinder called the inner electrode which is surrounded by a second metal cylinder called the outer electrode (see Fig. 1). Typically, the electrodes are machined from high conductivity metals such as copper or brass. The center electrode is sometimes hollow if axial optic measurements are required. Separating the two electrodes at the breech of the gun is an insulator made out of a high dielectric strength and mechanically strong material such as Pyrex glass or ceramic material. The barrel of the gun and the breech formed by the back vacuum end plate are enclosed in a vacuum chamber filled with a test gas, usually hydrogen or deuterium gas, at pressures in the .1 to 10 torr range.

After the chamber has been filled to the proper pressure, a high-voltage pulse is applied between the coaxial electrodes. Breakdown of the test gas occurs along the insulator and this breakdown essentially determines the shape of the ensuing plasma sheath. If the system is designed well, this initial breakdown will be radially symmetric and the developing plasma sheath will also be symmetric. The initial phase of the plasma generation is called the breakdown phase. Immediately after the thin plasma sheath is formed, magnetic forces cause the plasma to be accelerated forward along the axis of the electrodes in a classical electromagnetic shock tube acceleration mode. This phase of the dense plasma focus is called the

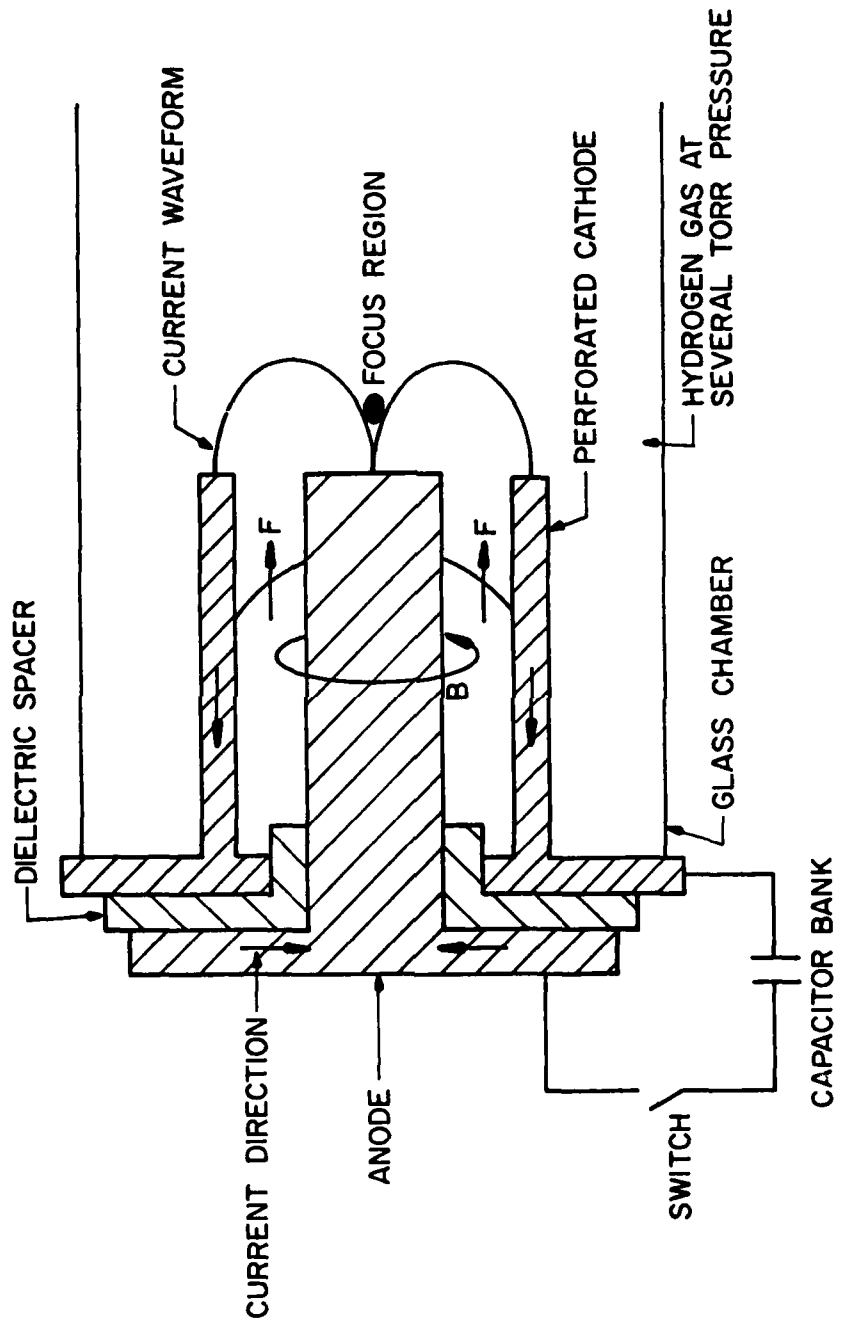


Fig. 1. Typical dense plasma focus apparatus.

acceleration phase. When the plasma sheath reaches the muzzle of the gun, the inner electrode no longer supports the plasma and magnetic forces cause the plasma sheath to constrict, pinching the plasma into a pencil-shaped dense plasma located a few centimeters from the end of the center electrode. This dense plasma pencil is a few millimeters in diameter and a few centimeters long centered on the axis of the device. Densities reach nearly 10^{+20} cm^{-3} with lifetimes nearly 1 microsecond long, much longer than predicted lifetimes. This final phase is called the collapse phase and is not well-understood.

2.1 Breakdown Phase

The initial breakdown has been found to develop from the center electrode along the insulator to the end-plate portion of the outer electrode when high voltage is applied between the electrodes. The breakdown takes place in several places around the insulator and the result is a radial, striated light pattern which forms a few tenths of a microsecond after application of the breakdown voltage. Polarity of the applied voltage does not appear to affect the formation of the plasma sheath.

The initial breakdown has a definite multifilamentary pattern, but appears to be cylindrically symmetric. As the current to the electrodes increases at a rate determined by the ringing frequency of the system, the filamentary pattern at the breech begins to move radially outward from the insulator until it reaches the cylinder part of the outer electrode. This effect has been called the inverse pinch effect because magnetic forces cause the plasma sheath to expand instead of pinch.

The reason for this expansion is diagrammed in Fig. 2. Figure 2a shows the initial breakdown across the insulator. When breakdown has occurred, the plasma carries current density indicated by the symbol \bar{J} .

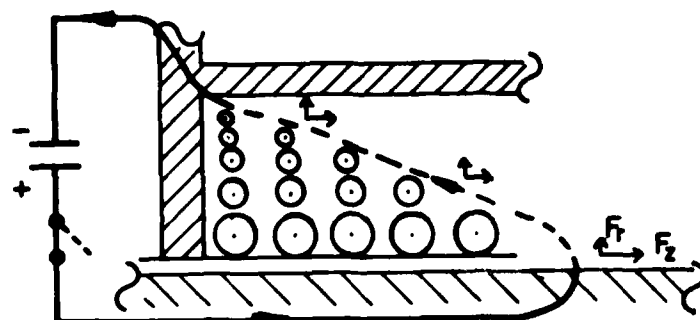
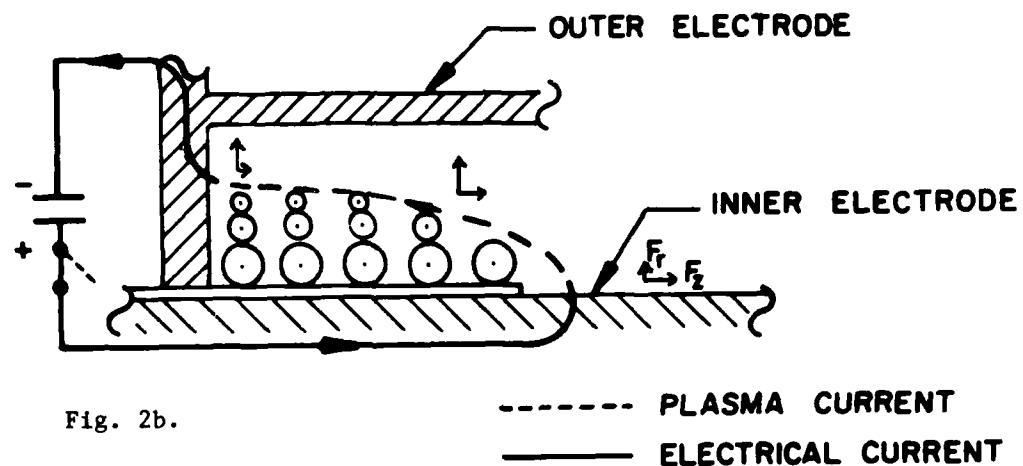
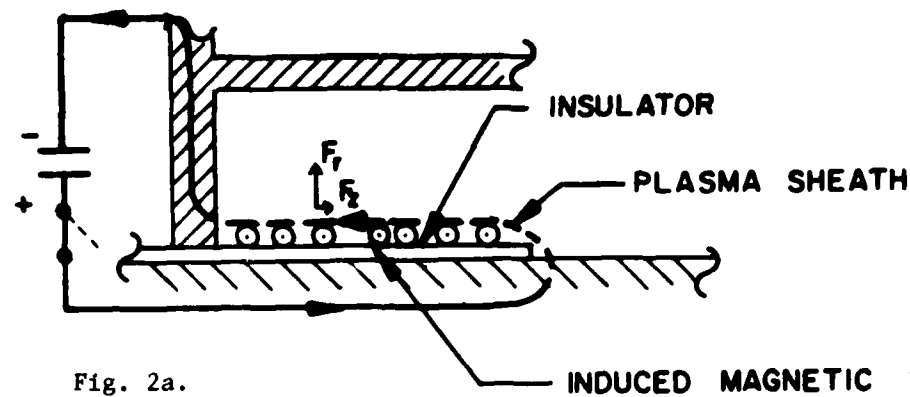


Fig. 2c.

Fig. 2. Dense plasma focus device breakdown phase.

The current flows through the plasma on the surface of the insulator from the center positive electrode along the insulator to the outer electrode end plate. This current produces a magnetic field inside the current loop according to Maxwell's equation, $\oint B \cdot d\ell = \mu_i$.

The magnetic field induced by the plasma current flows along the insulator, and in turn, creates a force acting on this same plasma current according to the force equation $\bar{F} = \int i d\bar{L} \times \bar{B}$, where \bar{F} is the induced magnetic force, i is the current, \bar{B} is the magnetic field, and $d\bar{L}$ is a very small segment of the current path. This force is mostly in the outward direction, as shown by Fig. 2b. This outward expansion of the plasma continues along the end-plate boundary until the plasma reaches the outer electrode. At this point, as shown by Fig. 2c, the current path is nearly as much perpendicular to the inner electrode as it is parallel. The effect of this straightening of the plasma front is that the plasma begins to experience a significant axial acceleration and begins to move along the barrel of the gun, reaching velocities of nearly 10^7 cm/sec.

The initial plasma sheath shape is, for the most part, dictated by the insulator. For a strong plasma focus with large x-ray and neutron production, the filamentary pattern must be radially symmetric and the filaments must blend to form a uniform radially symmetric sheath about 1 microsecond after high-voltage application. It has been experimentally shown [6] that if the current sheath does not become azimuthally symmetric but instead develops a preferred radial filament, the neutron yield from a deuterium-gas-filled plasma gun is very poor. It has also been experimentally demonstrated [7] that as the capacitor bank energy is increased, the filamentary pattern becomes a uniform current sheath earlier.

2.2 The Acceleration Phase

The acceleration phase begins as the symmetric current sheath, formed during the breakdown phase, bridges the distance between the inner and outer electrodes from the breech of the outer electrode to the inner electrode along the insulator (see Fig. 2c). Notice that the current sheath is canted backward from the center electrode to the outer electrode. At breakdown this backwards slope is due to the shape of the insulator, but as the sheath is accelerated along the barrel, this shape is perpetuated due to the radial dependence of the $\bar{j} \times \bar{B}$ force. The current sheath has both an outward radial component and a backward axial component. The radial accelerating force is the result of $(\bar{j}_z \times \bar{B}_\theta)_r$ where \bar{j}_z is the axial component of the current and \bar{B}_θ is the induced magnetic field. This force is outward and forces the current sheath against the inner surface of the outer electrode. The axial accelerating force $(\bar{j}_z \times \bar{B}_\theta)_z$ varies as $1/r$ across the annulus and results in higher sheath velocities near the center electrode. The radial dependence of the magnetic field follows from the coaxial current path relationship $\int \bar{B} \cdot d\bar{l} = \mu_0 I$ where $d\bar{l} = r d\theta$; thus, $\int_0^{2\pi} r d\theta B_\theta = \mu_0 I$ and $B_\theta \propto I/r$.

Actual measurements [3] using magnetic probes to determine passage of the current sheath have shown that the current boundary velocity is in fact higher near the center electrode than at the outer electrode. Without a perforated outer electrode, the radial force term would lead to a plasma pileup at the outer electrode surface and in time would reduce the effective annular spacing, Δr . Because of the parabolic shape of the sheath, plasma flows radially outward along the current front and will cause further plasma pileup and eventual stagnation of the plasma if the outer electrode is not

perforated. It has been found [6] that use of a perforated outer electrode prevents stagnation at the outer electrode surface and substantially improves quality of focus and neutron production.

It is interesting to note that examination of the $(\vec{j} \times \vec{B})$ forces at the inner and outer electrode boundaries reveals that at the center electrode the axial force is much stronger than the radial force due to the larger radial component of the current distribution at the center electrode. At the outer electrode, the situation is reversed with a stronger radial force. Thus the sheath at the outer electrode boundary will tend to be accelerated axially much less than at the inner electrode leading to a further canting effect. Also, since B_θ falls off at $1/r$, the forces at the outer electrode are even further reduced, leading to further canting. This expected increase in the slope of the plasma sheath is not seen in observations of sheath propagation which reveal a much reduced canting effect.

The reason for this lack of increasing axial separation between the inner and outer boundaries of the sheath is that the mass pickup by the sheath is a nonlinear function of the radius [3]. The sheath mass increases almost linearly with axial propagation for radial positions near the center electrode, but at the outer electrode, the mass pickup is almost nonexistent. Thus, the center electrode boundary of the sheath experiences greater mass buildup than the outer electrode which reduces the acceleration of the center electrode boundary, and the sheath does not show an increase in backwards slope as rapidly as first supposed.

This nonlinear mass buildup, together with the largely radial forces at the outer electrode boundary, is called the "snow-plow" effect, and a model has been developed to predict the behavior of such a plasma sheath.

The overall time for plasma sheath acceleration to the muzzle of the gun can be predicted using the velocity relation determined by Rosenbluth and Garwin [8] in their sheath model called the snow-plow "M" theory. This model predicts that the velocity of the sheath can be calculated from the relationship

$$v_s = (c^2 E^2 / 4\pi \rho_0)^{1/4} \text{ cm/sec}$$

where $c = 3 \times 10^{10}$ cm/sec, ρ_0 = initial mass density of the gas, and E = electric field between the electrodes. Assuming a cylindrical geometry, $E = \frac{V}{r \cdot \ln(r_2/r_1)}$ where V is the applied breech voltage, r is the radius of interest between the electrodes, and r_1 and r_2 are the inner and outer electrode radii, respectively.

This velocity relationship was shown to be very effective [3] in predicting the arrival times of the current sheath at the muzzle of the gun. Predicting the time of arrival of the current sheath allows tailoring of the dense plasma focus system parameters such as gas-filling pressure, applied voltage, and center electrode length to produce a plasma focus coincident with the maximum bank current. By synchronizing the focus with the maximum sheath current, the energy stored in the magnetic field, which drives the pinch phase, can be maximized, thereby increasing x-ray and neutron production.

Typical test results [9] for a deuterium-gas-filled dense plasma focus are shown in Fig. 3. The time axis of each graph starts at the initiation of the breakdown phase. The steady current rise shown in Fig. 3a is largely determined by the ringing frequency of the system, $f = \frac{1}{2\pi\sqrt{LC}}$, where C = bank capacitance and L = system inductance. More will be said about this in Sec. 4.1. After about 2.1 μ sec from initiation, the current experiences a sudden drop and slowly falls off. This sudden drop in current

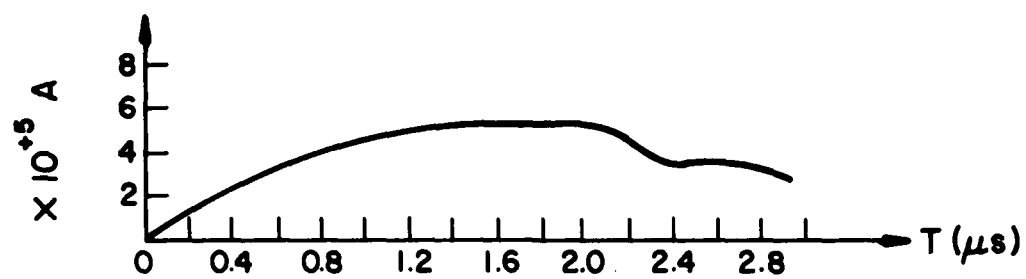


Fig. 3a. Sheath current.

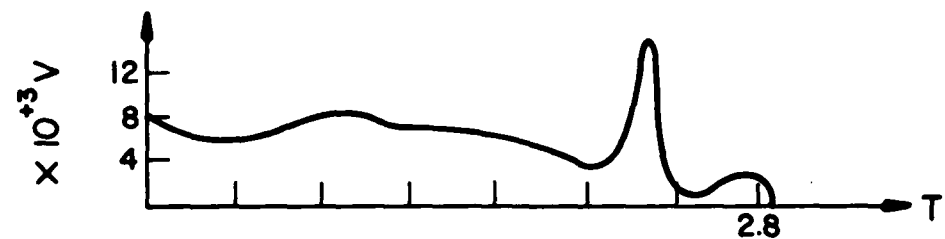


Fig. 3b. Breech voltage.

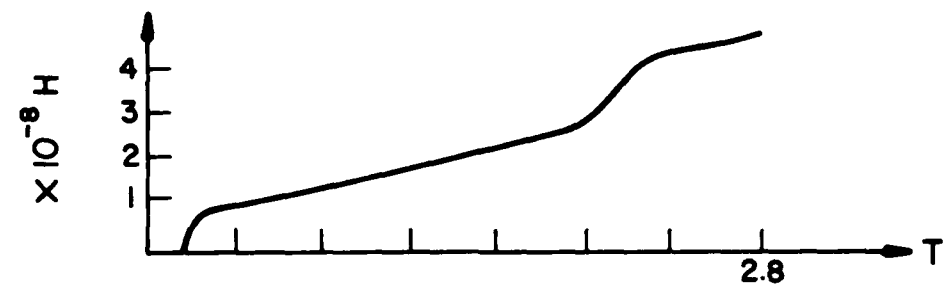


Fig. 3c. Device inductance.

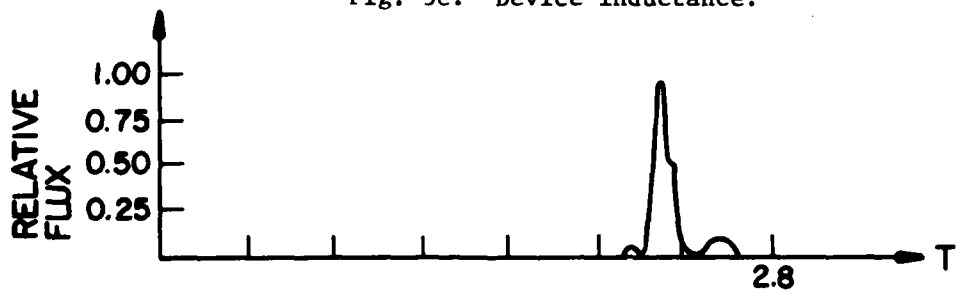


Fig. 3d. Neutron flux.

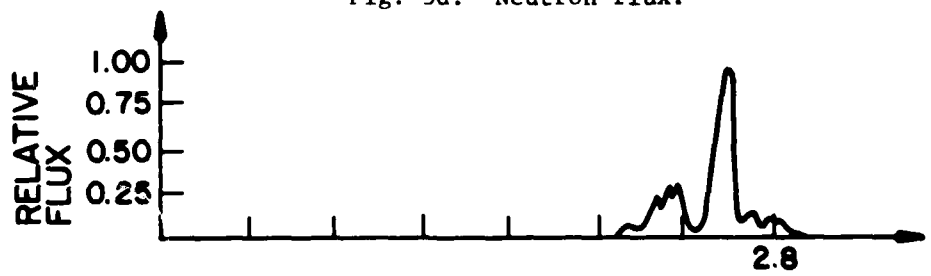


Fig. 3e. X-ray flux.

Fig. 3. Typical device waveforms.

is due to a rapid increase in internal inductance of the current sheath as the plasma sheath collapses due to lack of support from the center electrode as the sheath reaches the muzzle of the gun. A simple explanation of the increase in inductance is that the inductance can be defined by the following relationship: $L = \frac{\mu_0}{2\pi} \ln \left(\frac{r_2}{r_1} \right)$, where r_1 and r_2 are the inner and outer electrode radii, resulting in a large inductive increase as the inner radius decreases from a few centimeters to less than one millimeter when pinch occurs.

Note in Fig. 3b that simultaneously with the current drop the breech voltage experiences rapid increase due to $V = \frac{d}{dt} (LI) = I \frac{dL}{dt}$. The neutron and x-ray graphs also show a marked increase at this time, indicating that indeed this is the plasma pinch stage. Thus, sheath arrival times may be easily detected from the breech voltage and sheath current wave forms, and synchronization of the maximum current with the pinch may be accomplished.

Before leaving the acceleration phase, mention must be made of the gas removal efficiency of the plasma "snow-plow." Observations of photographs taken of the interelectrode space during and after pinch show no subsidiary breakdown between the electrodes indicating a rarified gas loading between the electrodes. Quantitatively, considerations of the Alfvén speed of the current front allow prediction of the gas density immediately following the front, and such calculations applied to the dense plasma focus [9] show that the gas density after "snow-plow" is reduced by a factor of 10^4 of the initial gas-filling density. Thus, the accelerating plasma sheath is a very efficient means of gas removal between the coaxial electrodes.

2.3 Collapse Phase

The collapse phase is by far the most interesting, but also the least understood portion of the dense plasma focus formation. The third phase

encompasses the rapid convergence of the plasma sheath to the axis and the conversion of stored magnetic energy to plasma energy in the focus. The two-dimensional radial and axial compression force offers no equilibrium along the axis, and plasma readily escapes axially in either direction. The very nature of the convergence causes much of the gas swept up by the plasma sheath to be ejected downstream and lost to the pinch. It is estimated [3] that the gas trapped in the focus is \sim 10 percent of the gas originally in the compression region. Even though the amount of gas trapped in the focus is relatively small, the pinch effect is perhaps the most efficient way of heating and compressing a plasma presently available. The pinch effect produces plasma densities of 10^{19} to 10^{20} cm^{-3} , x-rays near 500 keV, and neutron pulses of $> 10^{12}$ neutrons per pulse, when driven by large (multimegajoule) capacitor banks.

The production of x-rays remains obscure as current theoretical pinch models do not include a detailed x-ray production mechanism. Soft x-ray (< 7 keV) is emitted by thermal Bremsstrahlung from the focus region and hard x-ray originates at the surface of the center electrode and is caused by thick target Bremsstrahlung [10], [11]. As the inductance of the sheath increases during pinch, very large axial voltages are developed in the pinch region which accelerate electrons into the center electrode.

Experiments have shown [12] that a large percentage (> 90 percent) of the total x-ray energy appears as line emissions characteristic of the center electrode material. More recent experimental data [13] show an anisotropic hard x-ray distribution with a 75 percent increase in x-ray intensity between the angles of 38° and 75° from the gun axis, thus indicating a more complicated hard x-ray production mechanism than simple anode Bremsstrahlung bombardment.

When the dense plasma focus device is filled initially with deuterium gas, neutrons are produced in a pulse during the pinch, reaching magnitudes of 10^{10} to $> 10^{12}$ neutrons per burst. The pinch lasts about 100 nanoseconds, much longer than predicted by simple hydromagnetic theory. If the pinch phenomenon were connected with either a simple collapse-expansion mechanism or a sausage instability, one would expect that the lifetime would be on the order of a few nanoseconds. This expected confinement time is derived simply [9] from the time required for the ions to reach the center of the pinch which would imply infinite compression, obviously a maximum unstable situation. Dividing the pinch radius by the ion speed yields an estimate of stable pinch lifetimes. Typical values are 1 mm for the radius and 10^7 cm/sec for the ion velocity resulting in a confinement time of about 10 nanoseconds.

A working model of the dense plasma pinch must account for the longevity of the focus and also certain experimental data concerning neutron production. It has been shown [9], [10] that the neutron-flux is anisotropic with an axial neutron-flux shift in the 300 to 750 keV range indicating axial motion of the ions. In order to explain these unexpected results, several models of the dense plasma focus have been proposed. They can be described as follows:

(1) Ion Beam (Beam-Target) Model. According to this model, at the neck of the pinch very high electric fields generated by the collapsing sheath accelerate both electrons and ions to energies of several tens of keV. The ions strike the relatively stationary dense plasma near the focus, and thus produce neutrons from the ensuing collisions.

(2) Moving Boiler Model. In this model the collapse produces a relatively stable magnetohydrodynamic structure which moves axially away from

the center electrode. It is thought that this structure may be thermonuclear in nature.

(3) The Crossed-Field Model. This model is based on computing ion trajectories in a pinched plasma discharge. Theory predicts that high-energy ions are produced by acceleration in the crossed electric and magnetic fields generated by the rapidly constricting current distribution. These same crossed fields result in the high energy ions spending relatively short periods on the axis of the pinch, thus producing a smaller anisotropic neutron shift and accordingly smaller net plasma axial motion than the previous two models.

All three models offer a qualitative description of dense plasma focus mechanics, but only the crossed-field acceleration model seems to support experimental data. Figure 4a is a drawing which shows the Beam-Target model. The arrows indicate the supposed path of the ion beam. The first objection to this model lies in the resulting anisotropic shift introduced in the neutron yield from such a beam-target interaction. The resulting anisotropic shift would be greatest at a 45° angle to the axis, rather than at the axis as experimental data indicate. Second, to produce the required center of mass velocity of 10^8 cm/sec measured experimentally, the incident beam ions would require energies greater than 60 keV [14], much more energetic than temperatures measured experimentally. Electron temperatures are less than 10 keV and it is thought that the ion temperature is less than the electron temperature because plasma lifetimes are too short for the ions and electrons to achieve equipartition of energies [15]. Thus, it appears that the Beam-Target model is not valid.

The Moving Boiler model was introduced to account for the largely axial anisotropic neutron shift (see Fig. 4b). To produce the observed axial shift, the "boiler" must move axially at a velocity of 10^8 cm/sec.

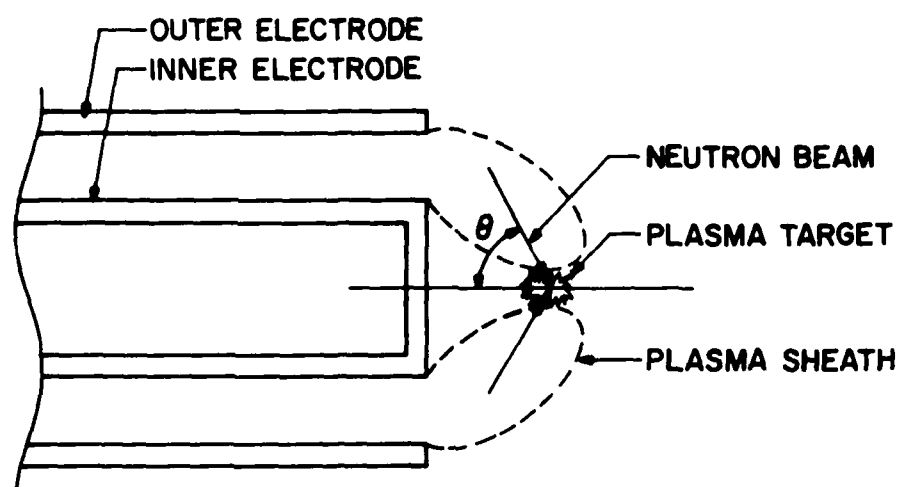


Fig. 4a. Beam target model.

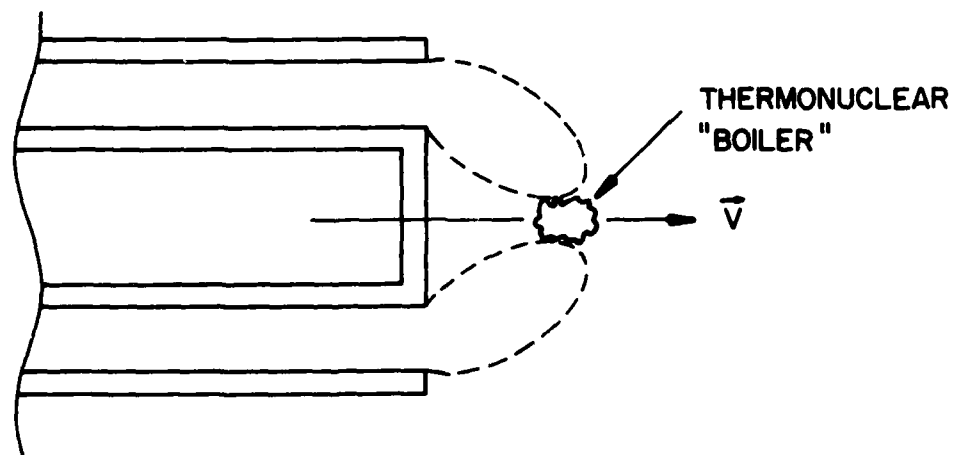


Fig. 4b. Moving "boiler" model.

Fig. 4. Fluid models of pinch mechanisms.

Also, to account for the magnitude of electron flux measured (up to 3.5 MeV) it is assumed that the "boiler" is thermonuclear in nature.

The first objection is obvious. The velocity of the moving boiler must be about 10^8 cm/sec and will lead to an axial "boiler" translation of nearly 10 cm for a pinch lasting typically 100 nsec. Such translations are not observed, and typical movements are from 2 to 4 cm [10]. Also, the 10^8 cm/sec velocity is difficult to explain because the maximum constriction velocity of the plasma pinch is 10^7 cm/sec, suggesting unknown accelerating mechanisms [16].

Second, the plasma focus does not appear to be dominated by thermonuclear neutron generation for two reasons. One, measured electron energy is around 3 keV and lifetimes of the plasma focus are such that equipartition of ion and electron energies is not attained; thus, the ions have less energy than the electrons with ion energies suspected to be < 1 keV [15]. Neutron energies this small indicate that the thermonuclear portion of the neutron generation is 1 percent or less [15]. Two, a detailed study of the neutron energy spectra provides additional evidence that the focus is not thermonuclear [16]. These experimental observations lead to a rejection of the first two macroscopic or "fluid" models of the plasma focus neutron generation.

The third model, the Crossed-Field Acceleration model, is a microscopic or "particle" model of the neutron production mechanism. This model was first developed by Bernstein [10], [16], [17], and later modified by Gary and Hohl [18]. Essentially, the Bernstein model accounts for neutron trajectories due to the $\bar{E} \times \bar{B}$ forces generated by the nonuniform plasma pinch. As the plasma constricts nonuniformly due to the driving magnetic field B_z , axial electric fields with radial dependence are produced due to $E_z \propto \frac{dB}{dt} \theta$. Reference [17] contains graphs of the radial

dependence of J_z (axial sheath current), B_θ , and E_z . Calculations of ion trajectories show that ions can be accelerated to energies of 200-600 keV following trajectories similar to the drawing in Fig. 5a [17]. The path of the ion loops back and forth in the azimuthal magnetic field crossing the axis at a range of angles. The path the ion takes is not a function of the initial energy but rather the angle of incidence upon entering the accelerating mechanism of the pinch. Since the magnetic field is zero at the axis, the ions spend more time moving at an angle to the axis than parallel to it. As the ion gains in energy, the path tends to smooth out and the ion proceeds in a largely axial trajectory as in Fig. 5a. The effect of all this is that the ion gains the most energy when moving at an angle to the axis but as it gains energy, the path of the ion will be axial, thus realizing the large axial, highly energetic ion beam needed to produce the noted anisotropy of the neutrons. In this way, ions are sufficiently energized but spend little time in axial motion, thereby resulting in the proper center of mass energy shift and yet still achieving the large observed neutron energies.

Gary and Hohl contend that Bernstein's particle approach is basically correct, but it suffers from a serious weakness. They note that the electric field generated by the nonlinear collapsing magnetic field should produce an axial electric field, but one that is largest on the axis, rather than off-axis as Bernstein's model predicts. A choice of $E_z(0) = 0$ implies strong electric fields radially away from the axis, leading to a cyclotron acceleration ion heating process. Gary and Hohl, however, feel it is more appropriate to choose $E_z(r) = 0$ outside the plasma in agreement with Lenz's law. This implies a strong induced electric field which is largest on the axis.

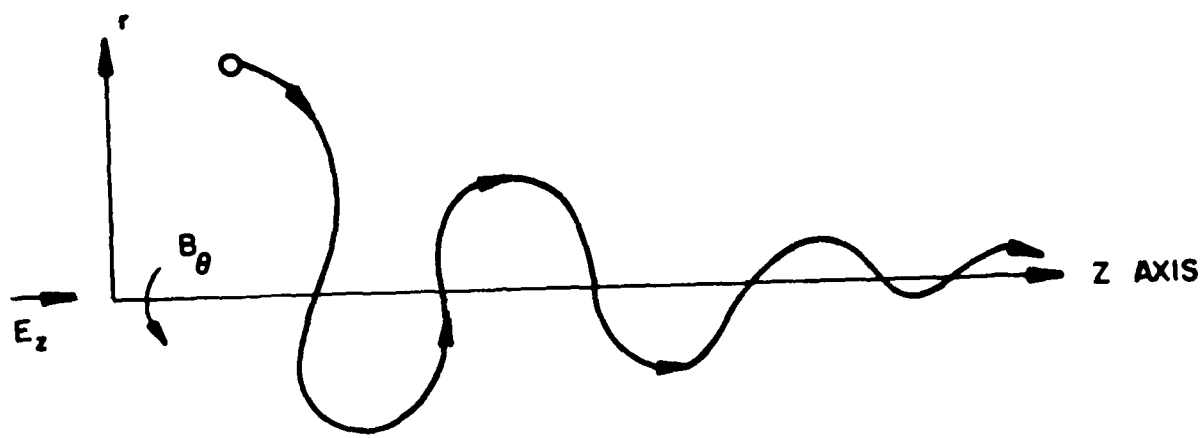


Fig. 5a. Bernstein model.

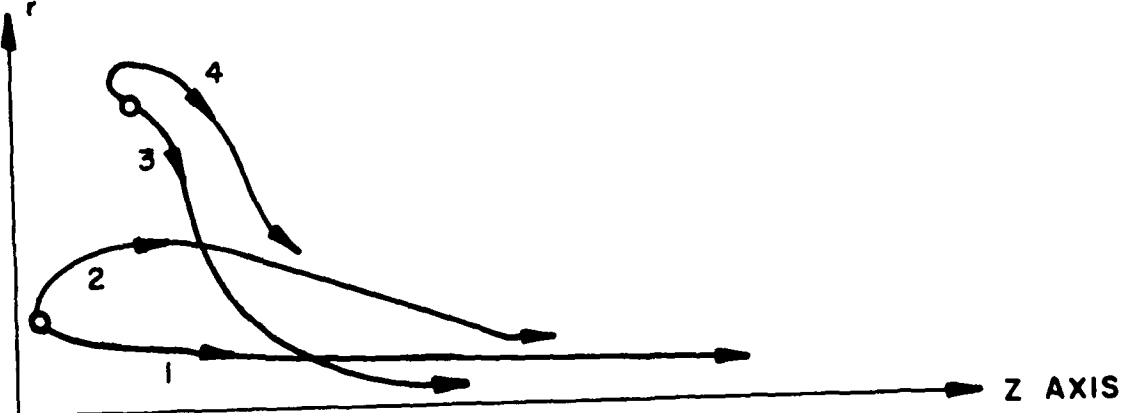


Fig. 5b. Gary-Hohl model.

Fig. 5. Ion trajectory models.

As the current drops, the changing magnetic field produces an axial electric field in the positive Z direction according to Gary and Hohl. This axial electric field not only accelerates ions in the direction of the observed neutron anisotropy, but provides an $\bar{E} \times \bar{B}$ drift toward the axis where the ions are most likely to gain energy from the electric field. This process is suggested to be a very efficient means of energy transfer to the ions. See Fig. 5b for a drawing of this model.

For large radii, the ions undergo cyclotron acceleration characterized by energy gain but little axial velocity gain. As the ion drifts to the axis where B_θ is small and E_z is large, the ion experiences axial streaming characterized by an axially directed energy gain. In this way, the ions are not simultaneously drawn into the axial ion stream, but rather the ions at small radii are pulled into the stream first, followed by the ions at larger radii as these ions drift to the axis. The net effect is an efficient heating process with only a small number of ions achieving high axial velocities at any one time.

In summary, the Crossed-Field Acceleration model of the pinch mechanism appears to be the most consistent with experimental data. It accounts for the neutron anisotropy, the neutron heating and the large observed neutron energies. This model also seems realistic when known pinch parameters are inserted in the model. It should be noted that the first two phases of the dense plasma focus can be modeled macroscopically, but the pinch phase appears to require a microscopic particle model of ion kinematics. Computer codes [19] have been devised, which are relatively accurate, except for the pinch phase, based upon fluid models. More detailed data are required to determine which models are correct to fully explain the dense plasma focus operation.

3. DENSE PLASMA FOCUS DEVICE DESIGN

Most experimental publications tend to abbreviate the experimental technique not directly related to the thesis, and by doing so, often make duplication of the experiment difficult and at times nearly impossible without much developmental experimentation. It is hoped that this paper will allow more rapid duplication of a dense plasma focus experiment by considering the detailed explanations of device design in the following chapters.

3.1 Mather- vs. Filipov-Type Device

Before the dense plasma focus device design could be formalized, there were several basic decisions to be made. First, the type of design, Mather vs. Filipov, had to be decided upon.

The Mather type is pictured in Fig. 1. This design is characterized by a long coaxial cylinder geometry with cylinder radii of roughly 5 cm and 10 cm, a ratio of cylinder diameters of approximately 2:1, and cylinder lengths of 15 cm to 30 cm.

The Filipov type is shown in Fig. 6. The most striking difference from the Mather design is the absence of a coaxial length to accelerate the plasma. The plasma is generated in the same way as the Mather device, and the pinch phase is similar, but the Filipov-type device lacks an acceleration phase. Immediately after breakdown, the plasma sheath sweeps along the outer electrode towards the axis and pinch begins almost immediately. The two devices produce similar results. However, the Filipov device is of considerably larger radial dimensions, being 48 cm for the inner electrode and 70 cm for the outer electrode.

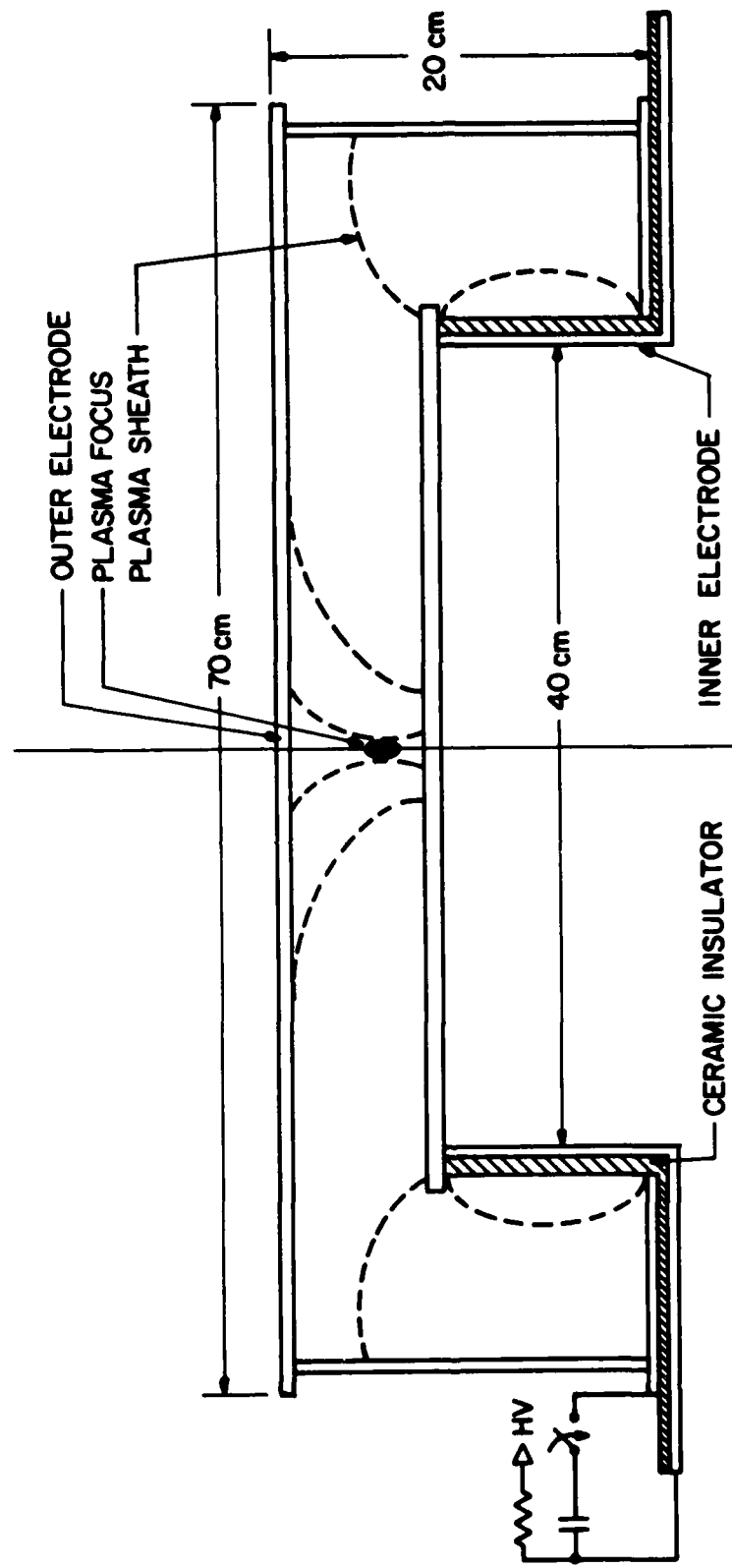


Fig. 6. Fillipov-type plasma focus device.

The vacuum system available for our experiments would have required considerable modification to house the Filipov-type device, but a system already existed consisting of a six-inch diameter Pyrex glass vacuum chamber in which to house the dense plasma focus device. It was felt that the smaller Mather type would be easier to handle, could be used with existing vacuum equipment, and would operate at lower storage bank energies. Therefore, the Mather type was chosen. That is not to say that the Filipov type was not equal to the Mather type; in fact, there is evidence [24] that the Filipov type may be the more efficient design. However, the logistics of the situation left no recourse except the construction of the Mather-type gun.

3.2 Dense Plasma Focus Device Configuration

Another subject for debate during the earlier stages of the design was device configuration. Several design variations have been tried by various groups and are shown in Fig. 7. Mather [3] tried the arrangement in Fig. 7a with the hope of stabilizing the axial flow of the plasma between the oppositely polarized center electrodes by using the two-gun arrangement shown. The system did not operate as expected, with almost no neutron production during synchronous firing, and relatively unstable plasma focus. A two-device system was a tempting configuration until this reference was discovered.

Figure 7b [20] shows another interesting geometry developed at the Aerospace Corporation. Using this arrangement, it was hoped that the shape would allow lower gas pressure loading at the breech with the mechanical arrangement providing additional compression at the muzzle. This interesting electrode configuration did not prove to be of any significant advantage.

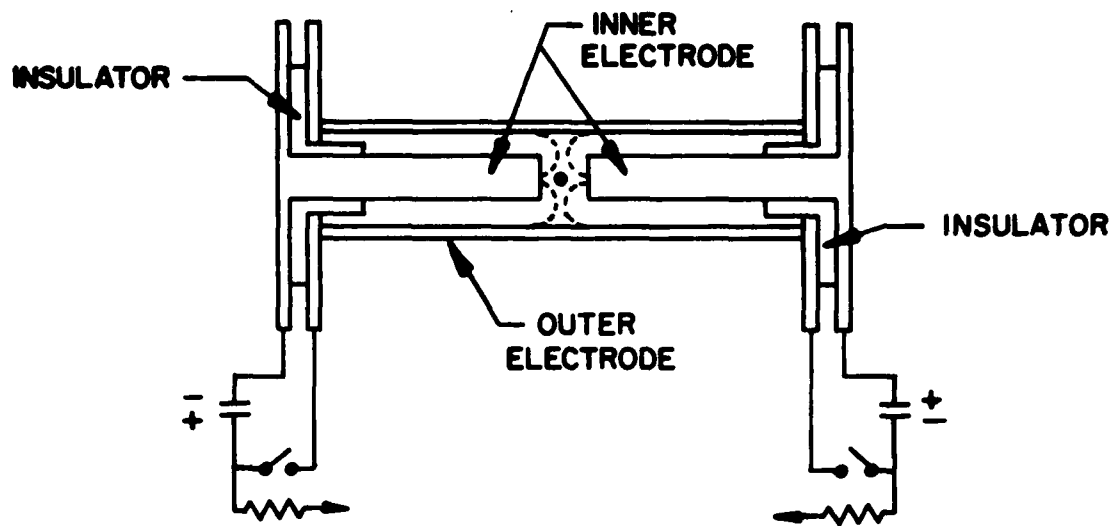


Fig. 7a. Opposing gun design.

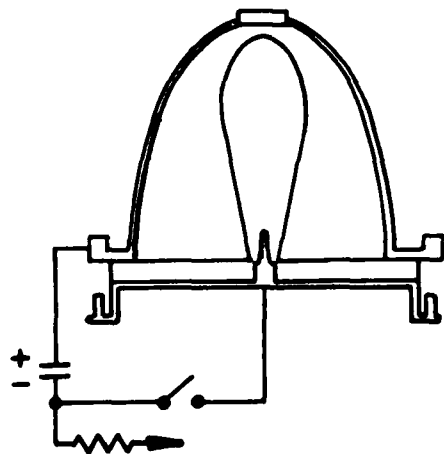


Fig. 7b. Parabolic design.

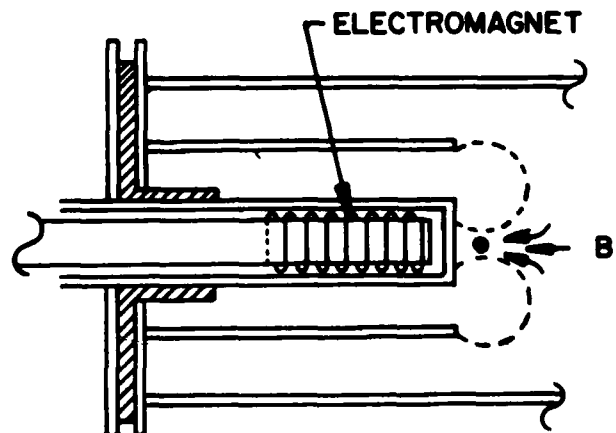


Fig. 7c. Coaxial magnetic field design.

Fig. 7. Various device geometries.

Figure 7c represents another attempt to stabilize the focus using an axial DC magnetic field. The magnetic field did in fact stabilize the focus, but at the expense of the x-ray intensity, resulting in an intensity reduction of several orders of magnitude [22].

These findings seemed to indicate that the standard geometry would be the most suitable for our experiments, thereby greatly reducing the already complex DPF system design task ahead.

3.3 Detailed Dense Plasma Focus Device Design

The dense plasma focus design for our experiments, which is shown in Fig. 8, consists basically of two coaxial cylindrical electrodes with a hat-shaped insulator between the electrodes to provide electrical isolation and also determine the initial shape of the plasma sheath. The electrodes are each fastened perpendicularly to a large metal disk which provides an electrical connection to each electrode and is a vacuum end plate as well. The outer electrode endplate forms a vacuum seal to a 6" diameter, Pyrex, cross-shaped vacuum chamber which houses the plasma gun and the x-ray diagnostics. A plexiglass end-plate spacer is placed between the end plates for electrical isolation and also to provide a vacuum seal between the inner and outer electrode end plates. When the electrodes are clamped together, the plexiglass spacer presses tightly against the electrode insulator forming a rigid assembly able to withstand the severe mechanical forces developed during the current impulse which drives the dense plasma focus.

A more detailed device design will now be presented in four parts: the outer electrode, inner electrode, end-plate spacer and electrode insulator designs. Each will be discussed in turn with a final discussion of miscellaneous device design considerations.

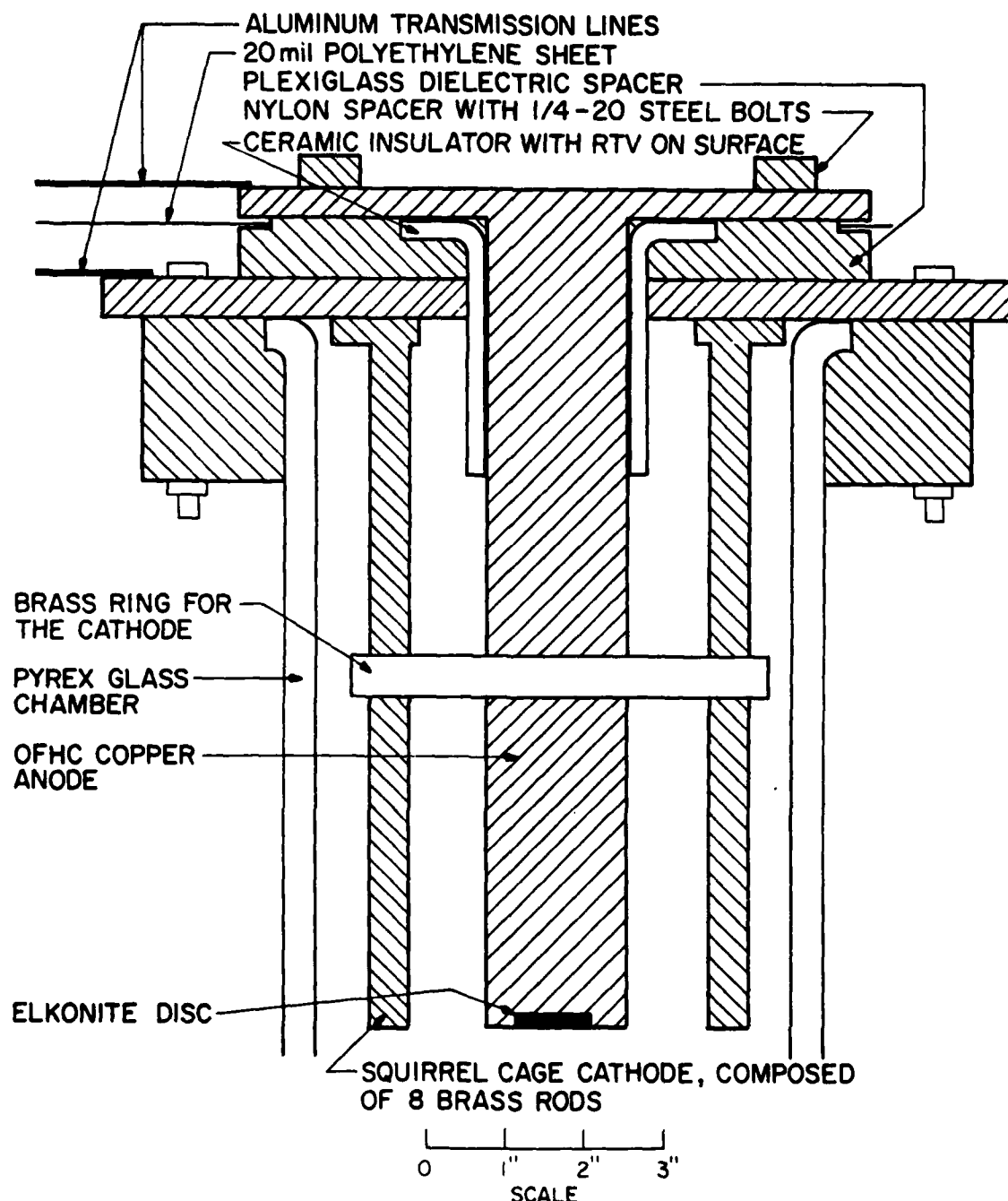


Fig. 8. Experimental dense plasma focus device.

3.3.1 The inner electrode design

There were four fundamental parameters considered before building the center electrode assembly. First of all, a decision had to be made as to whether the inner electrode would be adjustable in length. For optimum device operation the current peak of the plasma should coincide with the arrival of the current sheath at the muzzle of the gun. The arrival time may be approximated by the center electrode length divided by the average sheath velocity. Thus, by varying the length, the sheath arrival time can be tuned to the current peak. A movable center electrode would have required an additional complexity deemed unnecessary because the sheath velocity could also be adjusted, to a lesser degree, by varying the fill gas pressure and the applied voltage.

The second design consideration was the choice of a solid versus a hollow center electrode. Hollow center electrodes are used when optical diagnostics of the plasma focus are required and also when x-ray Bremsstrahlung of the center electrode tip is undesirable. The hollow center electrode is vacuum sealed at the breech end by a transparent window of various materials such as a salt window in the case of an infrared plasma probe. The decision was made to use a solid electrode because of simplicity and lack of a real need to use the hollow electrode.

The center electrode diameter was also a design parameter chosen for convenience because of the lack of any reference in the literature regarding the importance of this dimension. The center electrode was machined from a 2" diameter solid rod of OFHC copper with a finished diameter of 1.78". To reduce plasma erosion of the center electrode tip, an Elkonite disk, 3/16" thick by 1" diameter, was silver soldered into a recess in the center electrode tip and then faced-off flush with the surface of the tip.

Elkonite is a sintered material composed of tungsten and various percentages of silver, copper or silver carbide. The Elkonite used was grade 30W3, 80 percent tungsten and 20 percent copper by weight. This grade is particularly resistant to arcing and pitting, yet has good electrical and thermal conductivities.

The length of the center electrode, the fourth design parameter, unfortunately was relatively fixed by the geometry of the Pyrex cross-vacuum chamber which housed the gun (see Fig. 15, page 61). It was felt that an important consideration in determining the center electrode length was in placing the focus in the center of the Pyrex cross to allow a semiconductor detector to measure x-ray radiations. This length measured about 9" from the outer electrode end plate. A more rigorous estimate of the electrode length would have required knowing the risetime of the capacitor discharge system; then, for various pressures and bank voltages a sheath velocity could be estimated allowing the calculation of necessary lengths to time the sheath arrival with the maximum current from the bank. The exact bank parameters were not fixed at the time of device design, so it was felt that the bank could be designed to accommodate the required 9" length.

The center electrode, after being fitted with the Elkonite tip insert, was silver soldered into a recess cut in an 8" diameter, 3/8" thick brass disc which formed the inner electrode vacuum end plate. Eleven 1/2" diameter holes, spaced 30° apart on a 5.75" bolt circle, were drilled in the end plate with the twelfth position left blank and positioned at the bottom of the end plate for maximum electrical connection to the capacitor bank parallel plane transmission line. Nylon T-shaped bushings, 1/2" in diameter, were inserted in these holes with a 1/4" bolt piercing each bushing. The bolts were seated against 1" diameter shoulders that formed the top of the

bushings. In this way, the bolts were electrically insulated from the inner electrode end plate and yet could still clamp against the end plate by pressing against the nylon bushing shoulders. The bolts were screwed into threaded holes in the outer electrode end plate allowing the end plates to be clamped together forming a vacuum seal with the end plate spacer, which will be discussed in Section 3.3.3.

An early design used only six clamping bolts and it was discovered that the end plate clamping was not sufficiently uniform, thus unevenly stressing the insulator and allowing the discharge impulse developed during device operation to mechanically shock the end-plate assembly to the point of destruction of the electrode insulator.

3.3.2 The outer electrode design

The length, diameter, and the amount of electrode perforation were primary outer electrode design considerations. At the time of the device design, dense plasma focus literature did not indicate quantitatively the amount of perforation required, although some degree of perforation was almost always mentioned. A squirrel-cage geometry was finally adopted to minimize "snow-plow" buildup during the acceleration phase and also to allow optical recording of the wavefront if so required. The squirrel cage also reduced the weight of the device to allow one-man removal and installation of the device.

The diameter was chosen to provide a minimum annular spacing between the inner and outer electrodes of 1" or greater. Research by Mather [6] seemed to indicate that maintaining a 1" minimum annular spacing was necessary, and current designs almost without exception conform to this empirical criterion. Purely for reasons of convenience, our design was

given an annular spacing of 1.13". The length of the center electrode was chosen to coincide with the length of the inner electrode which extended 9" into the vacuum chamber.

The squirrel cage was composed of eight 1/2" diameter brass rods rounded at the muzzle end. The rods were evenly spaced with a 45° angle between the rods. The rods were silver soldered to a .35" thick, 5.75" outside and 4.3" inside diameter brass ring which provided support for the rods and also electrical connection to the rods from the outer electrode end plate by way of six evenly spaced 1/4" Allen head bolts, which screwed into holes tapped in the end plate, pressing the ring firmly against the end plate.

During plasma acceleration, magnetic forces generated by the plasma current exert an outward radial force on the outer electrode, causing the squirrel cage to expand, thus dissipating energy needed to drive the pinch. To reduce this loss, a brass ring, 1/2" thick with an annular thickness of 1.5", was constructed with an inside radius equal to the inside radius of the outer electrode. The rods passed through holes in the ring and were held in place by set screws in the ring. The ring was positioned about halfway down the gun barrel and not moved again.

The outer electrode end plate was constructed from 1/2" thick brass plate and given an outside radius of 11.5". Threaded holes were tapped in the end plate to match the inner electrode clamping bolts and the squirrel cage ring bolts previously discussed. Also, eight .4" diameter holes on a 9.375" bolt circle were drilled to provide bolt holes for clamping the end plate to the Pyrex vacuum chamber collar. A 2.4" diameter hole was drilled through the center of the end plate to allow clearance for the electrode insulator. The edges of this hole were rounded with a 1/4" radius corner to reduce the electric field intensity with the purpose of preventing dielectric breakdown of the electrode insulator.

3.3.3 End-plate spacer design

The end-plate spacer design required that the spacer provide a vacuum seal, electrical isolation and a rigid mechanical support between the end plates. To meet these requirements a disc-shaped plexiglass spacer was developed with a diameter of 8.5" and a thickness of 3/4", radially wide enough to fill the space between the end plates and thick enough to avoid surface tracking across the thickness of the spacer. Once again, eleven holes were drilled in the spacer to coincide with the end plate clamping bolts. Also, a circular recess, 1/4" deep with a 4" diameter, was machined in the plexiglass to fit the collar of the electrode insulator, and a 2" diameter hole was cut through the center of the spacer for the center electrode to pass through. O-ring grooves were machined into both sides of the spacer to coincide with identical grooves in the end plates, thus forming vacuum seals when Viton o-rings were inserted in the grooves, and the assembly was clamped together by the eleven clamping bolts. The spacer was rigid enough to withstand deformation caused by clamping the end-plate assembly together as evidenced by the lack of objectionable vacuum leaks during the pretest pump-down periods. During device operation, however, the violent mechanical forces applied to the end-plate assembly caused intermittent vacuum leaks on the order of .05 torr of impurity gas per shot. This did not occur often, and by tightening the end-plate clamping bolts again, the problem was often momentarily reduced. The existence of such a problem, however, indicates a problem with the end-plate clamping mechanism and possibly the choice of plexiglass as the end-plate spacer.

An alternative design might possibly be the construction of the spacer from the same material as the electrode insulator with vacuum seals cut in the collar of the insulator. The advantages are a reduction of parts and a more rigid insulator/spacer assembly.

3.3.4 The electrode insulator design

The design of the electrode insulator was a very critical part of the device and much experimentation was required to produce a useable insulator. The insulator material had to be mechanically strong, a good electrical insulator and also resistant to plasma erosion. Two available materials that met these requirements were Pyrex glass and Lava, a machineable ceramic. The first insulators were made from Pyrex because Pyrex was cheap and simple to work with. There seemed to be no difference in the sought-after qualities of the two materials so the decision to use Pyrex seemed a good one.

The Pyrex insulator was made from a Pyrex tube 0.10" thick with a 1.98" nominal inside diameter. The tube was slightly elliptical with a cross section whose axes varied the whole length of the tube. The ratio of major to minor axes had a maximum of 1.05. The portions used for the insulator were selected for maximum symmetry, but at best were still marginally round. An 8" long section of the tube formed the raw material for an insulator. The tube section was placed in a glass lathe and approximately 5" were heated until soft enough to flare the glass into a 4" diameter collar perpendicular to the tube axis with about a 1/8" radius bend at the tube. The tube was then cut to a length long enough to allow 2" of glass insulator to extend into the vacuum chamber along the surface of the inner electrode. After cutting, the insulator was annealed to reduce strains in the glass from the previous work done on the insulator.

There were many problems with this design. The method of forming the collar did not produce uniform fillets at the bends nor did it produce collars that were uniformly perpendicular to the tube axis. Also, the nonuniformity of the tube diameter allowed the tube to move when the device

was pulsed, and the resulting motion was a contributing factor in the destruction of almost every glass collar after only a few shots. In general, destruction of the insulator was largely initiated in the collar bend area with almost total pulverization of the collar the end result. The tube portion of the insulator was usually relatively intact with only a few long cracks.

Several attempts were made to nullify this mechanical shock destruction. First, Dow-Corning #4, a silicon high-dielectric grease, was used to coat the surfaces of the collar, forming a cushion for the collar. The grease did not work as expected and actually caused the insulator to destruct more easily. Various other shock-absorbing materials were tried and rejected with a final attempt using Viton o-rings as shock absorbers. Viton is 90 percent shock absorbing [22] so it was felt that a cushion made from Viton might provide a solution. The Viton cushioned insulators delayed but did not stop the insulator destruction, and the initial Pyrex insulator design was discarded.

It appeared that if the collar could be made more uniform and more nearly perpendicular the shattering problem might be solved. To meet these new collar requirements a new manufacturing technique was needed. One possible solution might have been to weld a glass tube to a disc-shaped collar cut from Pyrex sheet. In this way the collar would be uniform and the collar could be carefully fastened perpendicular to the tube. This design was not tried, however, because the decision was made to use a machineable hydrous aluminum silicate ceramic to manufacture the insulator. The ceramic could be machined with sufficient accuracy to produce a uniform perpendicular collar which could be made thicker to withstand the mechanical shock. The insulator tube section could also be made thicker for increased strength.

The end result was a hat-shaped ceramic insulator with cylinder walls .312" thick and 2.93" long with a collar .25" thick and 4.0" wide. The increase in thickness was dictated by the failure of earlier thinner ceramic insulators. After machining, the ceramic was cured at about 1000° C for six hours to strengthen the ceramic. Ceramic glazes were not tried, so it is not known what effect the insulator surface might have on device operation. The insulator did require a certain amount of conditioning, however, before the device would pinch. Conditioning is the process of repeatedly firing the gun until x-rays are detected from the focus region. It is suspected that the conditioning process is actually the deposition of short conducting paths on the insulator providing a voltage grading effect resulting in more uniform breakdown at the insulator [24].

3.3.5 Other device design considerations

Two other elements of the device design that are only indirectly related to the previous design discussion were discovered during development testing. The first design precaution is to provide adequate insulation between the electrode end plates. The second is the avoidance of exposure of easily ablated materials to the plasma.

As a further precaution against breakdown between the end plates, mylar sheet .040" thick was cut to cover the area between the end plates that was not already protected by the disc-shaped plexiglass spacer. Mylar has a high dielectric breakdown strength of greater than 4 MV/cm resulting in a breakdown voltage for the mylar end plate insulator of 400 kV, apparently more than enough for the magnitude of bank voltages used in the experiments. However, the breakdown strength of mylar is susceptible to minor surface damage. Also inductive changes during plasma focus may produce breech voltages exceeding five times the applied breech voltage; therefore, such a large margin of safety is not unreasonable.

It should also be noted that extreme care must be taken to totally remove easily ablated surfaces from exposure to the plasma. Upon contact with the high-energy plasma found in dense plasma devices, solid layers may vaporize, although it appears that metal vapors and ablated glasses and ceramics do not impair operation. Other device materials such as o-rings, nylon, and similar materials partly vaporize and ablate onto the electrodes causing erratic operation [23]. The device used in this experiment was designed to minimize this ablated contamination by removing all easily ablated materials from direct exposure to the plasma.

4. EXPERIMENTAL SYSTEM

The design of the dense plasma focus device is only a small part of the system design. A complete system is composed of an energy storage and transmission system, a high-energy switch, a vacuum and gas control system, instrumentation, shielding, grounding, and high-voltage charging circuitry, in addition to the dense plasma focus device. The goal of this overall design was to achieve an operational system at minimum cost while maintaining acceptable performance. In several instances, a more thorough design was theoretically possible had time and funds permitted. A discussion of possible improvements is presented to allow consideration of alternative designs. A block diagram of the experimental system is shown in Fig. 9.

4.1 Energy Storage and Transmission

The capacitor bank used for this experiment was a 43.5 μ F, 8.7 kJ (at 20 kV) bank composed of three 14.5 μ F Aerovox capacitors with individual internal inductances of \sim 89 nH. The ringing frequency of the bank alone was 143 kHz with a quarter cycle time of \sim 1.8 μ sec. Figures 10a,b show the capacitor bank arrangement and equivalent circuit.

The capacitors were seventeen years old and required high-voltage cycling to recondition each capacitor. This cycling was accomplished by charging each capacitor to several kV, then discharging each capacitor through a spark-gap shunt. Some capacitors required repeated initiation of the spark gap before the capacitor would discharge totally. The cause of this reluctance to discharge is unknown. Because of the age of the bank, capacitor explosions were feared and cycling was operated inside a 3/4" thick plywood box because plywood is an excellent explosive shock

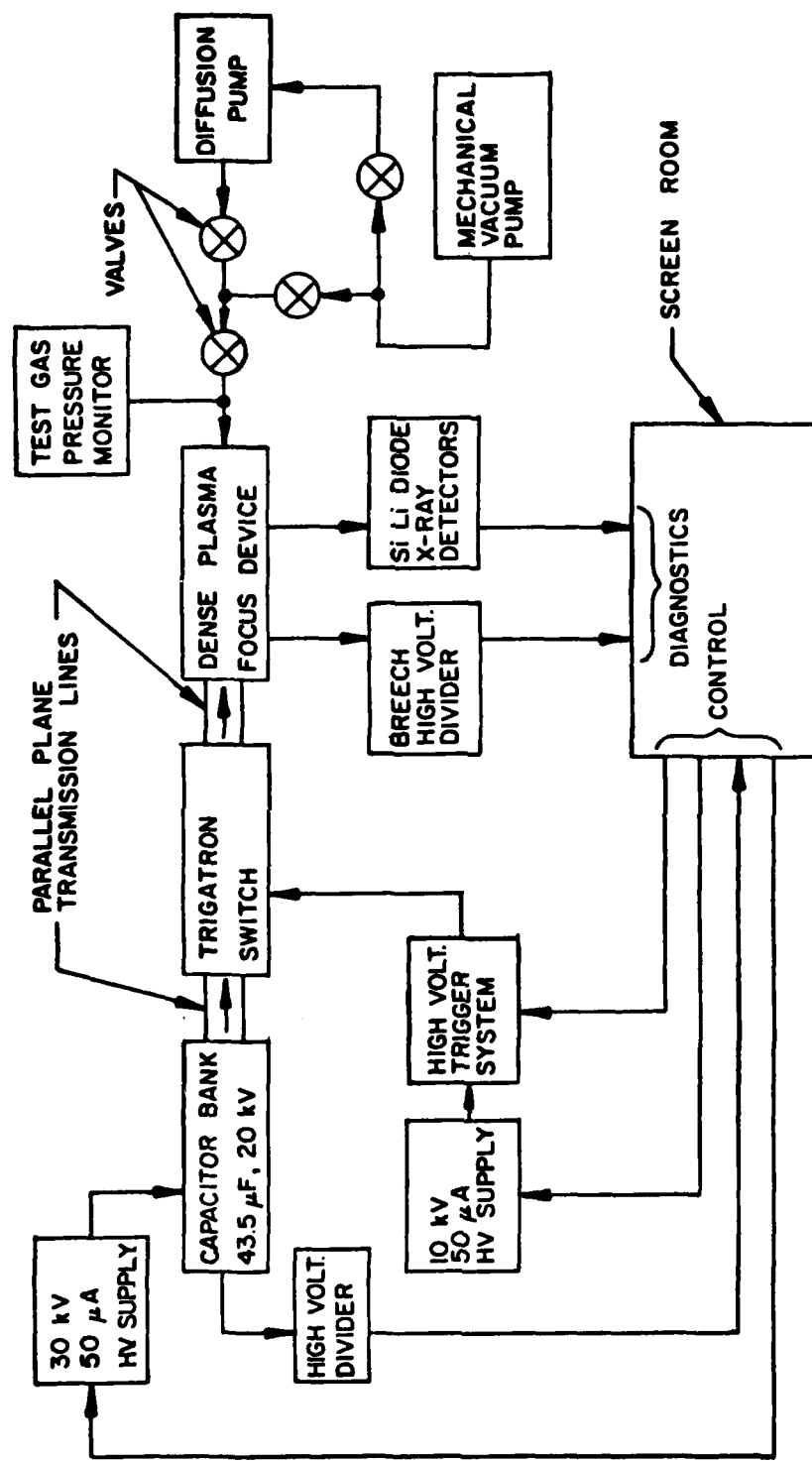


Fig. 9. Dense plasma focus experimental system.

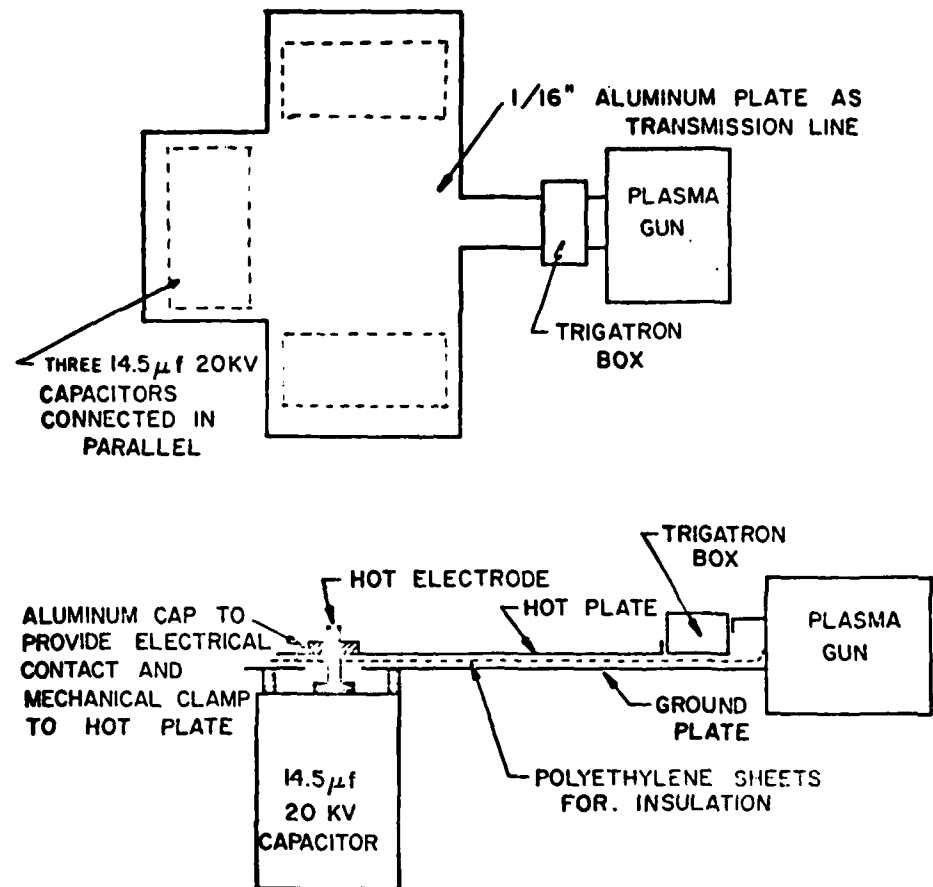


Fig. 10a. The capacitor bank arrangement.

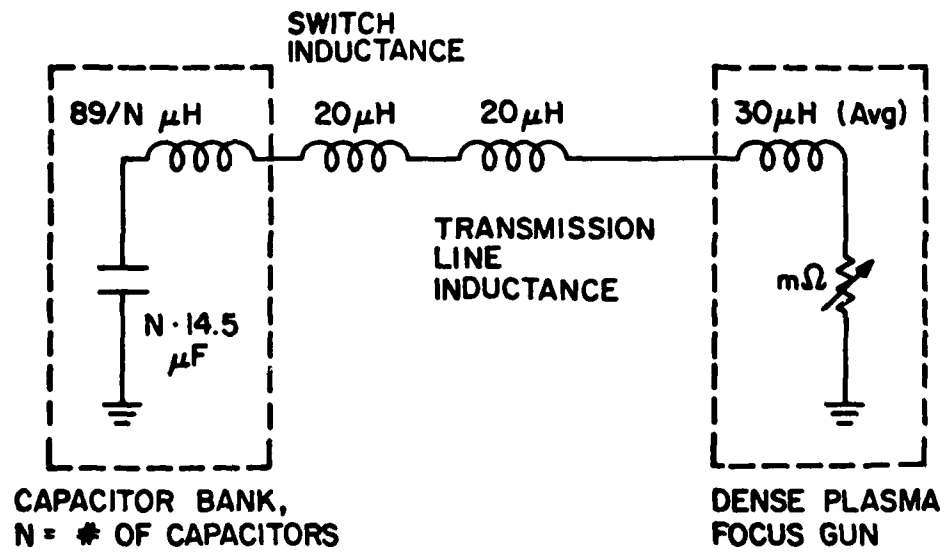


Fig. 10b. Equivalent electrical circuit of bank and gun.

absorber. In an effort to extend the life of the bank, the bank was operated below the rated 20 kV, as studies of capacitor lifetimes reveal that the lifetime of a high-energy capacitor varies inversely as the fifth power of the working voltage [25].

The capacitors had four 3/8" tapped holes on the top of each capacitor case, one hole at each corner, which comprised the negative grounded terminal of the capacitors. The positive lead was a 1/2" threaded post that pierced the case in the center of the top of the case and was insulated from the case by a 4" diameter circular porcelain bushing. For safety purposes, the capacitor cases rested on a 1/32" thick copper sheet grounded to single-point ground of the system. The copper sheet rested on a mobile plywood platform that could be wheeled away from the breech of the plasma gun for easy access to the gun. During operation the bank was enclosed in a 3/4" plywood box used both for protection from possible capacitor rupture and from the possibility of electrical shock to operating personnel from the lethal energies stored in the bank.

Satisfactory operation of the dense plasma focus requires prompt initiation of energy transfer from a high-current, low-inductance capacitor discharge bank. Also, to effectively transfer energy from the bank to the device, the bank impedance must be matched as closely as possible to the average impedance of the device which was about .03 ohm. To satisfy these requirements with modest cost, a parallel plane transmission line was used (see Fig. 10a). The cases of the capacitors were tied in parallel by bolting four lugs on the top of each capacitor case to a single sheet of 1/16" thick aluminum sheet. Three holes, 4" in diameter, were cut in this sheet to provide electrical isolation from the positive capacitor terminals. The 1/2" threaded positive terminals extended ~ 1" above the ground plate of the transmission line, and to these terminals, a threaded

low-inductance aluminum cap was screwed which pressed tightly against the upper positive plate of the transmission line to give the electrical connection to the upper plate. The upper plate was also 1/16" aluminum sheet and was perforated by three holes 1/2" in diameter through which the positive capacitor terminal passed. All metal edges were rounded to prevent unwanted breakdown.

The capacitors were arranged symmetrically around the 7" wide parallel plane transmission line feeder which connected the bank to the spark gap switch. To separate the plates, .020" of polystyrene sheet was used with a total electrical breakdown strength of 300 kV.

Measurement of the internal inductance of the capacitors was accomplished by measuring the capacitor ringing frequency when the transmission line feeder was shorted. This was done by removing the last 3" of insulation from between the transmission lines at the feeder end and then dropping the top feeder plate onto the bottom plate. A weight was attached to the top plate to reduce contact bounce when the plate was dropped. Measurements of the capacitor voltage showed a damped sinusoidal waveform. The period of the oscillation combined with the known capacitance can be used to calculate the internal inductance of the capacitors. The quarter-cycle time of the bank plus the transmission line not including the trigatron switch and the breech connections was about 1.8 μ sec. Typical plasma sheath velocity is about 5×10^6 in/sec; therefore, with the 9" gun length of our system, the sheath travel time would be about 1.8 μ sec. Adding to this time the initial breakdown time of about 1 μ sec, the total estimated delay from voltage application to the breech and formation of the focus is about 2.8 μ sec. The bank risetime was easily fast enough to produce maximum current by pinch formation, provided the external inductance was negligible.

This was not the case, however. Figure 10b shows the other inductance contributing elements of the system. The total system inductance was not due only to the bank, but was $L_{TOT} = \left(\frac{89}{3} + 20 + 20 + 30 \right) \text{nH}$, or about 100 nH. With a known capacitance of 43.5 μF , the average system ringing frequency was about 76 kHz. The quarter-cycle time was 3.3 μsec for the entire system, not optimum for the current peak to be coincident with the focus. Assuming a sinusoidal bank discharge with a current peak at 3.3 μsec allows an estimate of the magnitude of the current at 2.8 μsec or 85 percent of the quarter-cycle time. Such a calculation yields the interesting result that the current at 85 percent of the quarter cycle is about 97 percent of the maximum current, owing to the fact that a sine wave is slowly varying around the quarter-cycle times. Thus it was felt that the energy storage system risetime was sufficient to allow almost maximum current to drive the pinch.

These calculations are admittedly crude, but still illuminating. The discharge system risetime is crucial for effective coupling of the current peak to the focus formation. A previous bank with nine capacitors identical to the three used in the present bank produced very unsatisfactory results. Even though the energy storage was three times larger for the nine capacitor bank, the current risetime was also larger, having increased to 5.11 μsec .

The current is limited by the impedance of the bank plus the impedance of the gun, switch, and transmission line. For the circuit in Fig. 10b, the impedance at resonant frequency is $Z = \sqrt{\frac{L_{tot}}{C_{tot}}}$, where $L_{TOT} = \frac{L_{BANK}}{n} + L_{SWITCH} + L_{LINE} + L_{gun}$, and $C_{TOT} = n \cdot C_{BANK}$. The value n is the number of capacitors. The general formula for the impedance is $Z_n = \sqrt{\frac{L_B}{C_B} + \frac{L_S + L_L + L_g}{n \cdot C_B}}$. Calculating values for Z_n resulted in

$Z_3 = 8.8 \times 10^{-2}$ and $Z_9 = 8.2 \times 10^{-2}$. Increasing the bank energy by adding more capacitors only succeeded in increasing the maximum current by 7 percent but moved the current peak to 5.11 μ sec resulting in a net decrease in the current at pinch of 21 percent, largely because the current peak was shifted too far.

Three capacitors were optimum for maximizing current and still maintained a risetime close to the estimated sheath arrival time of 2.8 sec.

4.2 Fast High-Energy Switch

It has been found experimentally that satisfactory operation of the dense plasma focus device requires prompt application of large currents to the plasma at initiation of the breakdown phase. Recall from Section 2.1 that gas breakdown occurs across the insulator in isolated streamers that expand as plasma current increases until the striated pattern becomes a uniform sheath. Without a uniform sheath, the plasma focus will not form.

To insure rapid current rise, the inductance of the transmission line, breech connections, and the switch must be small so as not to seriously degrade the current risetime. In addition, the current must reach hundreds of kiloamps within the microsecond lifetimes of the operating device. Therefore, the switch must be low inductance, capable of carrying large currents, inexpensive, reliable, easily triggered, and with a geometry compatible with the system transmission line. The first two requirements are mandatory, but the remaining requirements allow some compromise.

4.2.1 Tube-type and mechanical switches

Tube-type switches were considered and immediately rejected. Tube switches, most notably thyratrons and ignitrons, are reliable, industry proven, and have well-characterized operation, but have relatively slow risetimes and are not able to carry the current load required unless many

devices are operated in parallel. For further discussion of tube switches refer to Reference [27].

Various mechanical switches such as solenoid and massive gravity-driven plungers were also considered, but were rejected because of suspected contact bounce and trigger jitter. Welding of contacts during high current passage was not considered a problem, as electrodes could be machined from arc-resistant materials such as Elkonite. The mechanical switch is almost ideal in all other respects. Such switches can be made low inductance, easily triggerable, inexpensive, and capable of conducting large currents. Mechanical switches of the gravity-driven massive plunger type have been used as impulse bank switches, but it was felt that our experimental system may at some time require more carefully controlled triggering. Therefore, electrical discharge initiated switches were studied and, as a result, a simple, reliable, and relatively low-jitter switch of this type was constructed.

4.2.2 Electrical discharge initiated switches

The remaining class of switches considered for the system was basically switches closed by means of an electrical discharge through a gaseous, solid, liquid or vacuum dielectric medium. Liquid gap switches are somewhat difficult to use because of explosive pressure buildup in the liquid during large current flow and because of erratic self-breakdown voltages caused by trapped bubbles, density gradients and impurities [28]. Because of these undesirable characteristics, the liquid dielectric switches were rejected.

4.2.2.1 Vacuum spark gaps. Vacuum spark gaps are inherently complex, requiring a gap enclosure capable of maintaining a vacuum of 10^{-5} to 10^{-7} torr during the explosive conduction of the gap. Vacuum gaps, however, offer the following advantages:

- (1) High dielectric strength
- (2) Rapid deionization time
- (3) Wide voltage range
- (4) High current capability
- (5) Low inductance
- (6) Quiet operation.

The design of vacuum spark gaps is not straightforward, and the obvious advantages must be weighed against several inconvenient design considerations. First of all, the ultimate breakdown voltage of the gap is greatly dependent upon the electrode surface conditions, which may vary the breakdown voltage by as much as 108 percent [29]. Thus, it is not practical to attempt to control the breakdown voltage accurately by electrode spacing. This electrode surface roughness effect is a major consideration when using data from vacuum breakdown measurements to design low inductance, hence, minimum spacing, vacuum spark gaps.

Another consideration when designing low-inductance spark gaps is the prevention of flashover along the external surface of the gap. The switch electrodes are so closely spaced in a low-inductance gap that unless special care is taken, breakdown will occur along the outside surface of the gap vacuum enclosure. Often this outer surface is immersed in transformer oil or a high-pressure electronegative gas. Interior dielectrics must be low-vapor-pressure materials that will not degrade the gap vacuum but will provide high dielectric strengths. Porcelain, ceramics and glass are often used. The gap vacuum is typically maintained by an active pumping system with a cold trap for oil pumps to remove oil contamination. Also, dielectric spacers are often inserted between the electrodes to cause the current to flow around the dielectric spacers, thus forcing the current to flow in a large cross-sectional area, further reducing inductance.

The major difficulty with vacuum gaps, other than the inconvenience of maintaining a vacuum, is triggering complexity. Spark-initiated gaps require relatively high pressures of 10^{-1} to 10^{-3} torr to provide enough molecules to supply charge carriers once they are ionized. The firing delay time is a strong function of the pressure and gap voltage, as well as trigger and electrode polarity [30]; thus, spark-initiated devices may have inherently long delays. Plasma injection is another method of triggering vacuum gaps, but such trigger devices tend to be complex. Lasers have been used as vacuum spark-gap triggers but require very high power lasers.

A vacuum spark gap has many advantages, but is complex to design, construct and maintain, and for these reasons was rejected in favor of a more simple, easily maintained switch.

4.2.2.2 Solid dielectric spark gap. Solid dielectric switches offer all the advantages of the vacuum dielectric switch with the exception of a self-healing dielectric. The solid dielectric switch, however, is simple, inexpensive and is easily triggered. The disadvantage of a nonhealing dielectric dictates the replacement of the switch dielectric after each switch closure, which will prohibit high repetition rates. For switching applications with relatively long cycle times, the solid dielectric switch may be suitable.

Triggering is accomplished by puncturing the dielectric, causing breakdown. Puncturing may be accomplished by electromechanical methods with microsecond jitter times or by electrically exploded foil or wire with nanosecond jitter times. The latter method has the disadvantage of requiring the replacement of both the dielectric and the trigger after each closure. A crude and relatively erratic triggering mechanism is to

simply overvolt the gap. This method may be somewhat enhanced by partially prepuncturing the dielectric to a uniform depth, thus providing a more consistent breakdown voltage. For certain applications this method offers the simplest and least expensive low-inductance switch available.

Triggered multielectrode solid dielectric switches are typically composed of one or more foil or wire electrodes sandwiched between solid dielectric sheets that are positioned between the switch electrodes. Puncture of the dielectric may be achieved simply by driving a ball point punch through the dielectric as shown in Fig. 11a. Before puncture, the trigger electrode is biased equipotentially between the switch electrodes. After puncture, however, the ensuing breakdown between the trigger electrode and the bottom electrode causes the trigger electrode to attain the same potential as the bottom electrode, thus greatly overvolting the upper gap causing the switch to close. Field distortion is also used in place of the ball punch as the trigger mechanism, as shown in Fig. 11b. The trigger electrode, normally biased equipotentially between the switch electrodes, is pulsed by a voltage large enough to cause dielectric breakdown between the bottom electrode and the trigger thus suddenly bringing the trigger to the potential of the bottom electrode. The gap between the trigger electrode and the top electrode is then severely overvolted causing complete switch closure.

Explosively triggered switches use a similar geometry, but instead of an electromechanical puncture mechanism, use the piercing force of either explosives or an electrically exploded metal foil. This method provides rapid closure but requires the replacement of both the trigger mechanism and the dielectric, greatly decreasing the firing rate.

Other factors affecting switch operation are electrode surface conditions, the switch package and surface contamination of the dielectric.

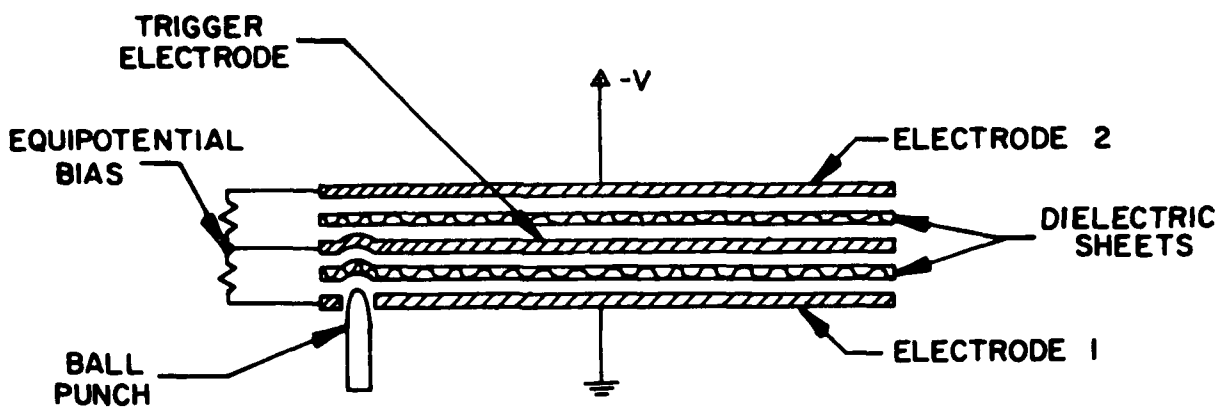


Fig. 11a. Ball punch trigger.

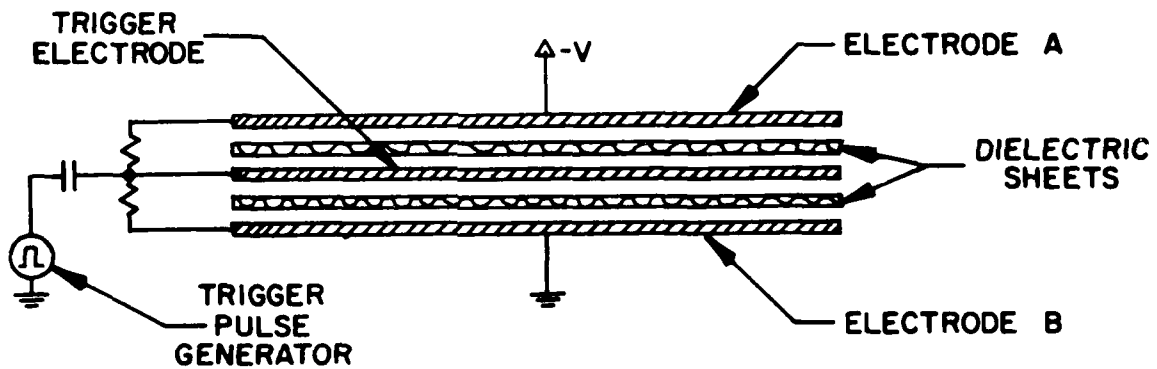


Fig. 11b. Field distortion trigger.

Fig. 11. Solid dielectric switch types.

Often the dielectric is submerged in transformer oil to reduce surface tracking and somewhat reduce switching noise [31]. To initiate multiple arcs between the switch electrodes, the trigger must have a risetime less than the arc formation time. It has also been found experimentally [28] that suitable channel formation occurs for $0.3 < q < 0.6$ where $q = Y/(X + Y)$, Y = dielectric thickness between the ground electrode and the trigger, X = dielectric thickness between the $-V$ electrode and the trigger.

4.2.2.3 Gas dielectric spark gaps. Gas dielectric switches have all the advantages of the vacuum and solid dielectric switches with two disadvantages. First of all, for low inductance the gap must be pressurized to increase gap breakdown voltages to allow minimum gap spacing. Pressurization will increase the cost of construction and maintenance of the switch. Second, several of the gases used for higher breakdown voltages such as SF_6 and fluorocarbons combine to form toxic vapors when high currents are passed through them. Other gases commonly used where very low inductance is not needed are air, N_2 , and CO_2 , which are inexpensive and relatively carefree.

The simplest type of gas dielectric switch is the overvolted gap in which the voltage applied to the gap increases until the gap breaks down. Such a gap has poor synchronization characteristics when used by itself, but when the voltage applied to the gap has a fast risetime and is much greater than the self-breakdown of the gap, then the switch closure is rapid with jitter in the nanosecond range. The overvolted gap is often used as a steeping gap or as a crowbar switch to guard against transients [32] and other overvoltage conditions.

An improvement in synchronization and a reduction in jitter and delay can be achieved by using a third trigger electrode to initiate breakdown, either by field distortion or by both ionization and field distortion.

The midplane trigger of a field-distortion triggered gap shown in Fig. 12a. is normally biased equipotentially between the gap electrodes. The gap is triggered by pulsing the trigger with a voltage large enough and steep enough to cause rapid and low jitter breakdown between the trigger and electrode A. As breakdown begins, the trigger is pulsed again but in the opposite direction, causing the gap between the trigger and electrode B to break down, thus closing the switch. The placement of the trigger relative to the gap space is in the proportion of from 60/40 to 70/30 [33], depending upon the total switch package. The requirements for the trigger pulses are severe for nanosecond jitter switching, with leading edge rise-times at least 4 kV per nanosecond [34], and for high-voltage switches the trigger voltages may be nearly as large as the holdoff voltage of an entire switch.

The trigatron form of the three-electrode spark gap switch initiates closure by ionization and field distortion. The third electrode is usually a pin inserted coaxially and electrically isolated from the host electrode as shown in Fig. 12b. A voltage pulse of a few kV to several thousand kV is applied to the trigger pin causing breakdown between the host electrode and the trigger, producing ionized charge carriers to be introduced into the switch gap leading to rapid switch closure.

The trigger mechanism has been studied elsewhere [35]-[38] and will not be discussed in detail; however, one important design consideration is electrode polarity [35]. The results of such a study, which are shown in Table 1 [35], are for gaps operated in excess of 40 percent of the static breakdown voltage of the gaps. For gaps operated at lower voltages, the trigger currents must be much larger to sufficiently ionize the gap. Also, lower voltage switches require trigger voltages that are a substantial portion of the gap voltage.

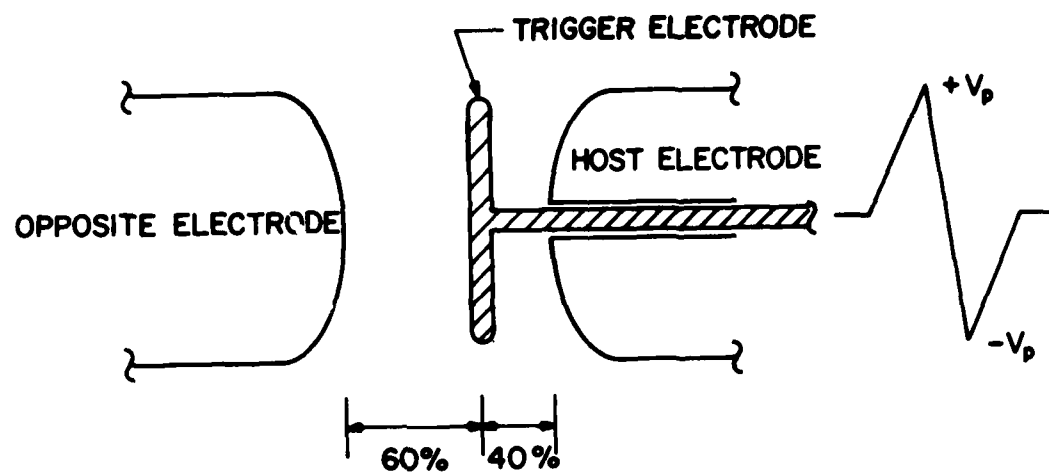


Fig. 12a. Field distortion trigger.

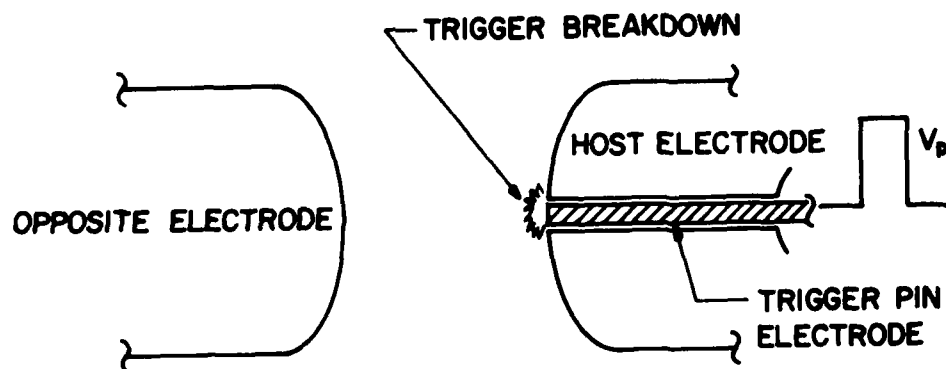


Fig. 12b. Trigatron switch.

Fig. 12. Gas dielectric switch types.

Trigatron gaps are well-characterized and have been designed for a wide range of voltages and timing requirements. The trigatron gap is easily triggered, can be operated in air, can operate at voltages in the range needed by dense plasma focus devices, and can be designed for low jitter, short delay and moderately low inductance of tens of nanohenries. In short, the air dielectric spark gap was the best compromise for our dense plasma focus high-energy switch.

4.2.3 System switch design

The trigatron-type air dielectric spark gap was chosen as the system switch because of low cost, triggering ease and simplicity of construction. The present design, however, evolved as a consequence of the failure of an earlier energy storage system design. The initial storage design consisted of a capacitor bank composed of ten 14.5 μ F capacitors in parallel arranged in five groups of two capacitors per group with a trigatron switch for each group to reduce the overall inductance of the switches. Parallel plane transmission lines connected the groups to a center parallel plane collection plate which fed directly to the plasma gun. Many problems were encountered using this design, and after much frustration, it was dismantled. The primary problem was synchronous ignition of the switches. A very fast risetime high-voltage trigger was required to effectively synchronize the triggers, but the development of such a trigger generator would have required a major expenditure of time and money. A simpler solution to the synchronization problem was simply to remove the problem by directly connecting all the capacitors in parallel and switching the total bank through a single trigatron switch. The latter solution was adopted and has proven adequate. The present experimental setup is shown in Fig. 10a and a detailed diagram of the switch is shown in Figs. 13a,b.

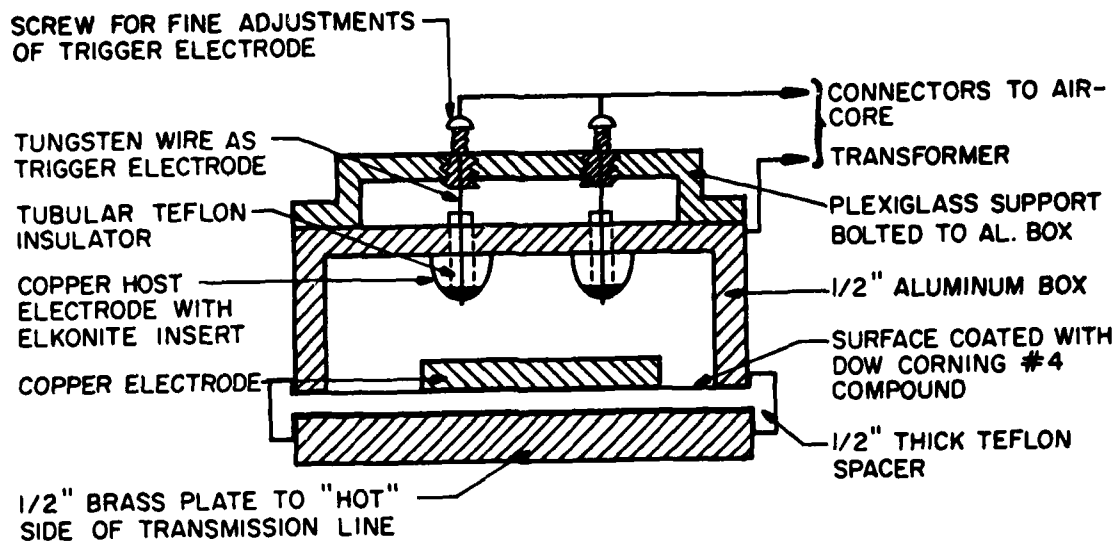


Fig. 13a. The front view of the spark gap.

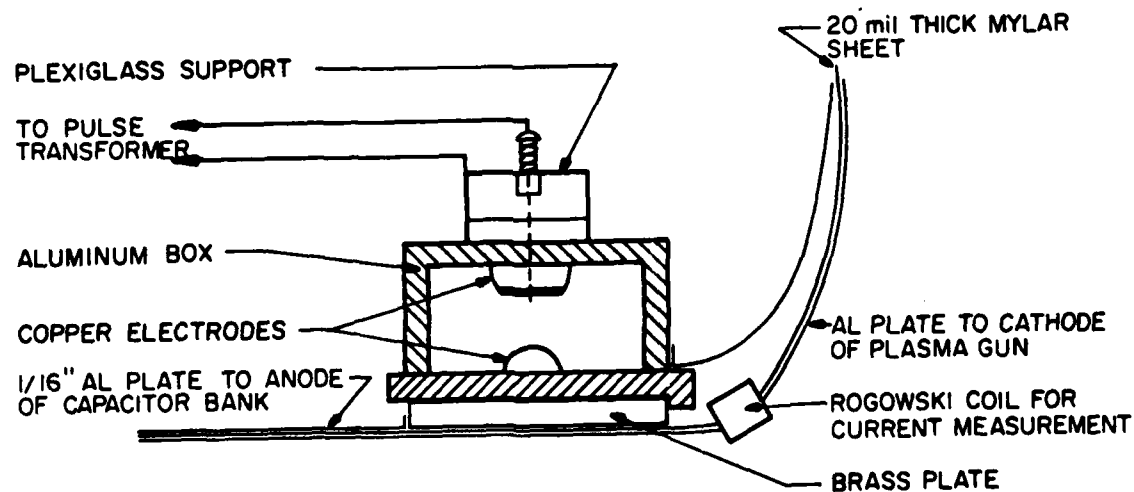


Fig. 13b. The side view of the spark gap.

The system switch is basically composed of two hemispherical upper electrodes pierced by tungsten trigger wires and a single hemicylindrical bottom electrode long enough to provide an opposite electrode surface for both upper electrodes. The electrodes were machined from 2" diameter OFHC copper and the upper electrodes were machined and fitted with Elkonite disks 1" in diameter and 3/16" thick. The upper electrodes were also drilled and tapped to accept 1/2" diameter steel bolts used to clamp the electrodes to the aluminum housing. The bolts were also drilled to provide a 1/4" diameter hole through which a cylindrical teflon insulator was inserted to insulate the trigger from the host electrode. At the Elkonite surface a .063" diameter hole was drilled to provide an ignition gap between the host electrode and the .050" tungsten wire. The switch housing was composed of 1/2" thick aluminum plates which formed a six-sided box. The upper plate was drilled to provide entry for the steel electrode clamping bolts. The bottom electrode was silver soldered to the bottom plate of the housing and measured .93" high and 5" long. The bottom plate was electrically insulated from the top of the housing by a teflon spacer and the whole assembly was rigidly clamped to reduce switching noise and offset internal pressures caused by the large current flow in the air gap. After clamping, the electrode gap spacing measured .39" providing a static breakdown voltage of about 20 kV.

The teflon spacer geometry used in the switch was developed to provide long breakdown paths between the edges of the upper and lower switch housing and also to center the upper housing with respect to the lower plate. Consistent alignment of the electrodes is important for repeatable switch operation. After repeated operation of the switch, it was found that a fine, powdery, reddish-brown grit coated the teflon surface and it was feared that surface degradation would become severe enough to cause

flashover of the insulator. To reduce teflon contamination, the insulator was coated by a thin film of Dow Corning #4 high-dielectric silicon grease which could be easily wiped off when contamination grew severe and a new layer reapplied.

Switch closure was initiated by pulsing the trigger electrode with a 14 kV pulse causing breakdown of the trigger-host electrode gap. The breakdown was so severe that a bright flare of ionized gas was ejected toward the opposite electrode even without a voltage applied across the main gap. The polarity of the trigger pulse did not affect switch operation, but for convenience, the trigger was operated with a positive polarity.

The jitter of the switch was measured to be 20 nsec with a trigger delay of about 200 nsec. The inductance of the switch was measured by discharging a capacitor with known inductance through the switch into a low-inductance load, and then measuring the ringing frequency of this RLC circuit. The circuit resistance was very small and could be ignored. The circuit capacitance was due to the storage capacitor applied to the switch and shunt. The shunt was constructed to provide an inductance of about 1 nH and could also be ignored. The remaining inductance in the circuit was due to the internal inductance of the capacitor and the unknown inductance of the switch. Thus by measuring the ringing frequency, the switch inductance could be calculated from the relationship $L_g = \frac{1}{(2\pi f)^2 \cdot C} - L_{cap}$ where L_g is the switch gap inductance, C is the storage capacitor's capacitance, and L_{cap} is the capacitor's internal inductance.

Such a measurement yielded a switch inductance of 20 nH. The breakdown voltage of the gap was much greater than 20 kV, so some improvement in inductance might have been possible by narrowing the switch gap. This was not done because the breakdown voltage is greatly affected by the temperature and humidity of the air [39], so some safety factor was deemed necessary.

To somewhat reduce the dependence of the breakdown voltage on air conditions, the gap was flushed continuously by a dry air flush from a high-pressure air bottle.

4.2.4 System switch trigger

The switch trigger system was required to provide a fast risetime, high-voltage pulse to the trigger electrode of the trigatron switch with a repeatable delay and low jitter upon command from either automatic timing circuitry or manual initiation. The circuit eventually developed to meet these requirements is shown in Figs. 14a,b.

The interface from a manual switch or various triggering devices to the pulse amplifier circuit was provided by a Tektronix type 161 pulse generator and a type 162 waveform generator which allowed control of trigger delay, waveshape and amplitude to the pulse amplifier. The pulse amplifier thyratron tube, type 2D21, was triggered by a 25-volt pulse from the 161, causing the 2D21 to rapidly conduct, effectively coupling the 100-ohm output resistor to a .05 μ F storage capacitor. The output of the pulse amplifier was a sharply rising 350-volt pulse with more than enough voltage to trigger the 5C22 high-voltage power thyratron with low jitter.

The anode of the 5C22 was connected to a 2 μ F high-voltage capacitor which was connected in series to the primary of a stepup high-voltage transformer. At this stage of the trigger cycle the 2 μ F capacitor had already been charged to the desired trigger level, typically 7 kV. Because the 5C22 load was an LC oscillating circuit, three fast high-voltage diodes with reverse breakdown voltages of 7 kV were connected to the 5C22 anode in a reverse bias configuration to shunt negative voltages from the LC load to the 5C22 anode so as not to exceed the 5 kV reverse-bias tube specifications.

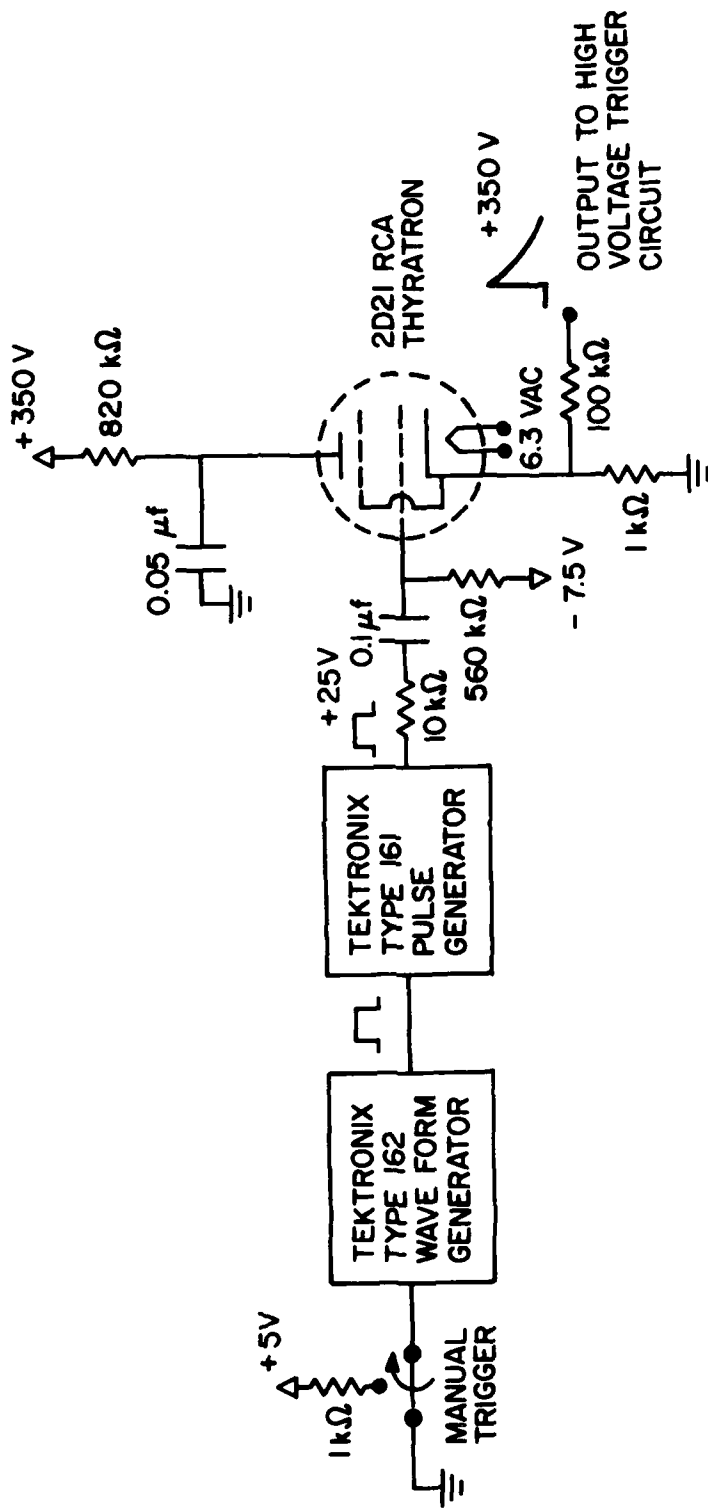


Fig. 14a. Pulse amplifier.

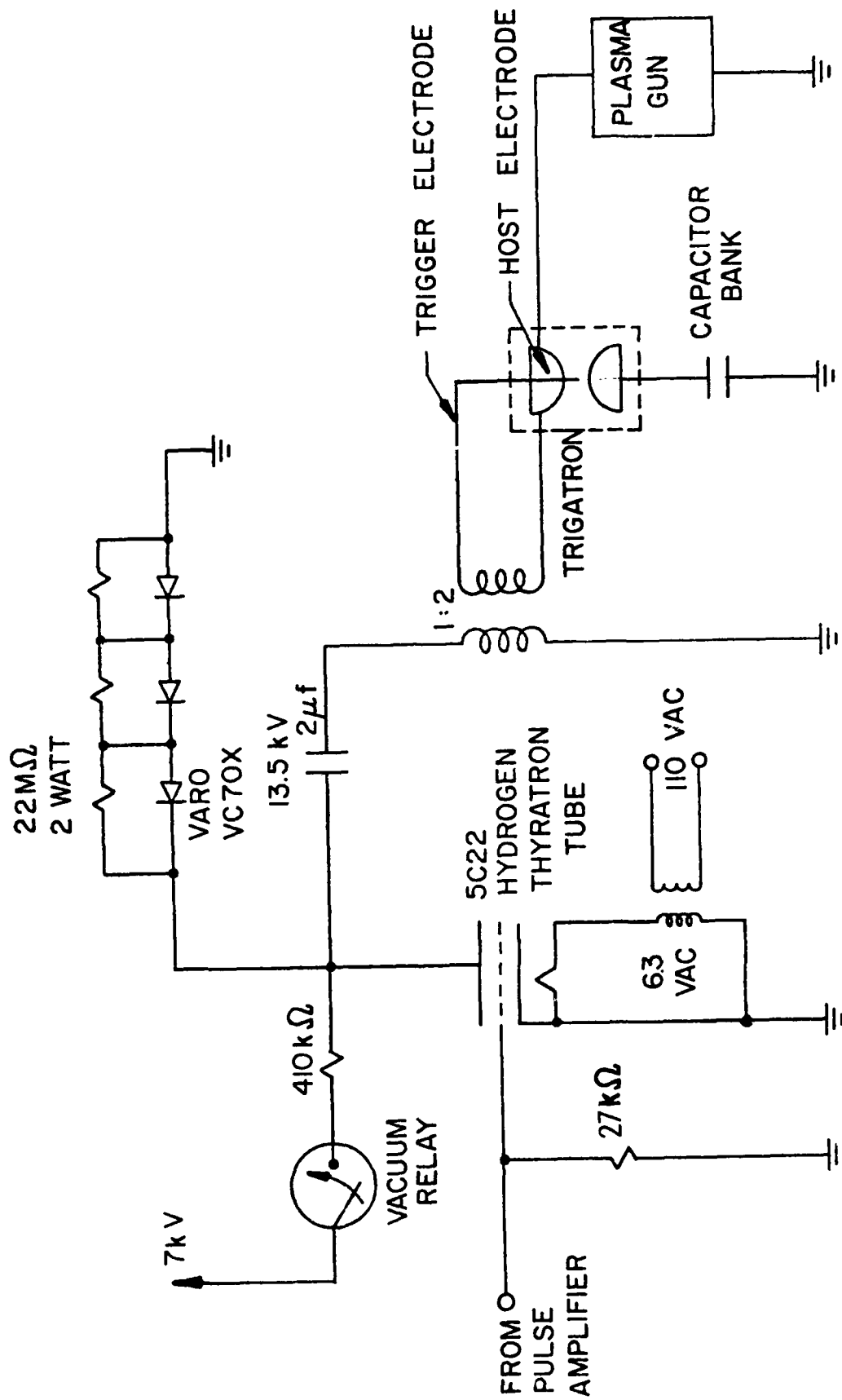


Fig. 14b. Triggering circuit for the thyratron tube and spark gap.

The pulse transformer was constructed from unshielded 30 kV breakdown high-voltage wire wound around a 2" diameter plexiglass tube. An air core was used to achieve the high-frequency response required and also because the air core will not saturate as most magnetic core materials will. Due to the air core and the relatively thick high-voltage insulation on the transformer windings, the magnetic flux coupling was poor and the actual turns ratio was 2.9:1 to achieve a voltage gain of 2:1. The windings were also scatter wound to lower the inductance of the transformer to improve the risetime of the transformer.

When the 5C22 was triggered, the 2 μ F capacitor was discharged through the 5C22, and the current through the 5C22 also passed through the transformer primary. This current caused a voltage to appear at the secondary connected to the trigatron trigger pin, causing the switch to break down and close. The isolation provided by the transformer allowed the trigatron trigger to be pulsed with either polarity trigger pulse and also decoupled the trigger circuit ground from the high-voltage switch. This trigger circuit performed reliably and satisfied the trigger system requirements.

An earlier trigger circuit design using TTL logic circuitry in place of the 161 and 162 to provide timing, interlock detection and semiautomation of the device operation proved unsuccessful. The original trigger circuit plans called for the correlation of external events with the trigger pulse and programmable delays synchronizing external events and devices such as counters, oscilloscopes, and other experimental apparatus. The concept was ambitious but was not realized due to an unsolved prefire condition in the TTL trigger circuit.

Basically, the initial circuit was composed of a series of TTL monostable multivibrators, called one-shots, connected in series forming a delay line with taps that could be switched to various outputs for control and timing. The output of a selected one-shot fired a trigger pulselwidth control one-shot which in turn fired a Schmidt trigger level shifter. The output of the Schmidt trigger was capacitively coupled to the 5C22 grid, causing the 5C22 to conduct. Used separately, the TTL and Schmidt trigger worked reliably and the 5C22 was capable of holding off up to 16 kV for hours if necessary. However, when the circuits were connected, charging the 5C22 would cause the TTL to fire when the charge voltage reached about 4 kV. One attempted solution involved total isolation of the various circuit grounds and the use of bypass capacitors where possible, all with no detectable change. The solid-state electronics were also placed in a carefully shielded housing with no improvement noted. Various logic schemes were tried to cancel the prefire effect, to no avail. The power supplies were also doubly filtered without any effect.

The investigation into the causes of the prefire condition was very time-consuming, and rather than waste more time, it was decided that an all-tube circuit with inherent higher noise thresholds and larger noise coupling impedances would be constructed and the solid-state trigger circuit would be abandoned. Possible solutions that were not tried but could possibly have provided the isolation needed are optical isolation devices and/or pulse transformers. These two methods of decoupling the high-voltage circuitry were difficult to implement because of the unavailability of these devices within a reasonable time. It is not known why the high-voltage circuitry caused the TTL to prefire. One can only conjecture that because of the low 1-volt noise immunity of the TTL, a small percentage of noise in the high-voltage circuitry was more than enough to trigger the TTL one-shots.

4.3 Vacuum and Gas Control System

The vacuum source for this experiment is composed of a Veeco vacuum station, type R3-3A with a diffusion pump, liquid nitrogen cold trap and a standard mechanical vacuum pump (see Fig. 15). This system is capable of pumping the plasma focus chamber to 10^{-6} torr within eight minutes. The mechanical pump is relatively slow, requiring the bulk of the pump down-time. The diffusion pump is manually switched into the system when the pressure reaches about 40 torr and quickly pulls the vacuum down to 10^{-6} torr. The liquid nitrogen cold trap is necessary to contain the diffusion pump oil to prevent backstreaming of diffusion pump oil vapor into the vacuum system.

The system was initially pumped down to 10^{-6} torr to keep the percentage of contaminating gas to a low level. The operating sequence was simply to pump down to the 10^{-6} torr range, then close off the plasma chamber from the vacuum station. Once the plasma chamber was isolated, the test gas was bled into the chamber at pressures in the 0.1 to 10 torr range. Thus impurities from previous gas fillings are estimated to be only one part in 10^6 .

The plasma chamber consisted of a 6" tube diameter Pyrex cross with the ports of the cross loaded as shown in Fig. 15. Semiconductor x-ray detectors were placed at 90° to the plasma gun axis. Also in the vacuum end plate opposite the plasma gun were connections to the test gas-filling apparatus. An Airco vacuum gate valve was used to close off the vacuum station from the plasma chamber. To decouple mechanical shock from the plasma chamber to the vacuum station, two 4" diameter steel bellows were used between the vacuum station and the gate valve.

Glass vacuum systems are often composed of many short sections pieced together like a plumber's nightmare. These sections are at times difficult

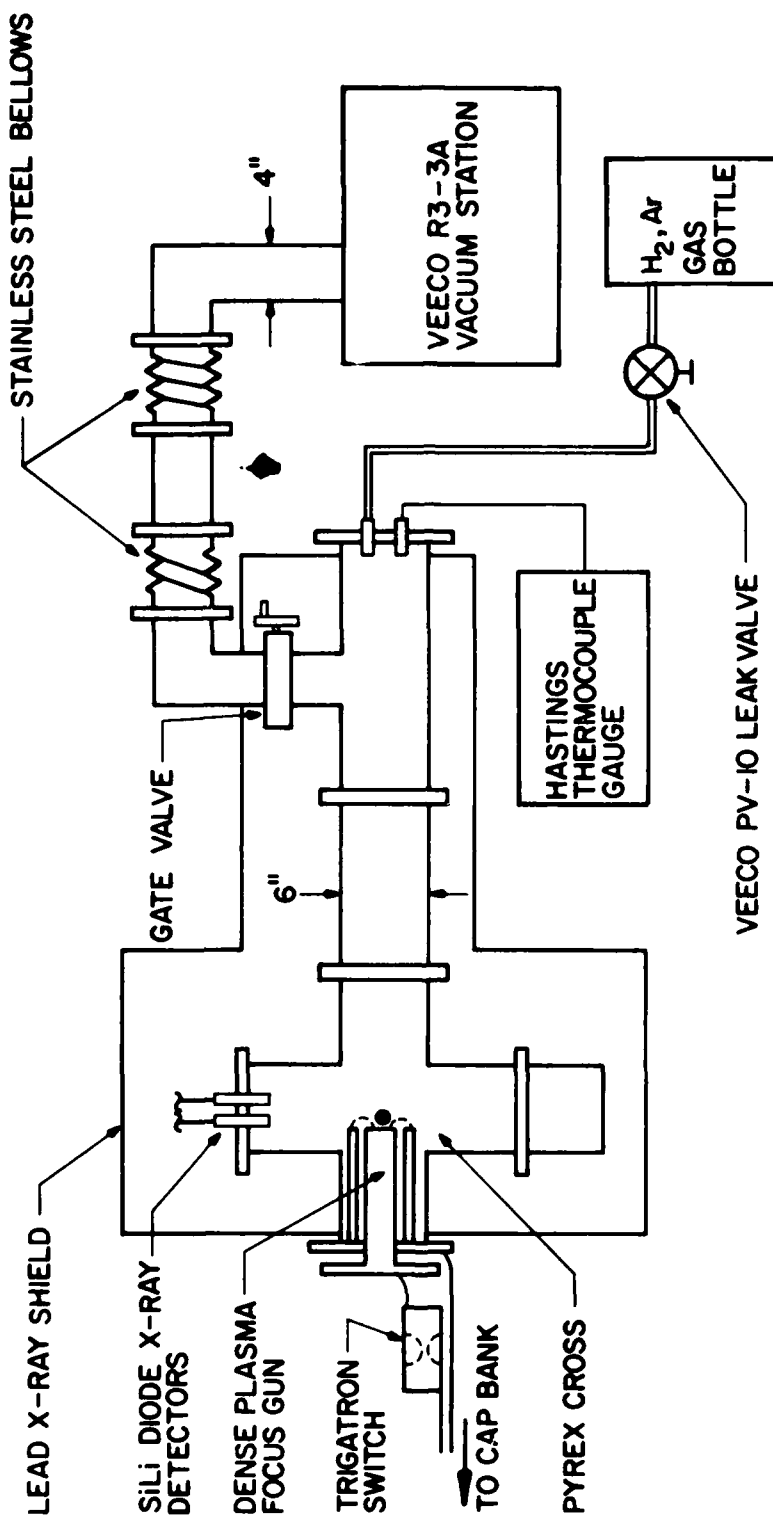


Fig. 15. Vacuum system.

to align for a proper vacuum seal and the sections must be carefully supported so as not to overstress the glass joints. Glass was used here only because it allowed easy access for optical measurements of the plasma focus and because it was readily available. Metal chambers can and have been used successfully for dense plasma focus experiments and are preferable because the metal chamber can be grounded, thus reducing electrical shock danger, the metal chambers are less susceptible to mechanical breakage, and the metal chambers are usually custom made, which allows the designer to minimize vacuum connections and reduce the volume of the vacuum chamber to a minimum. Care should be taken, however, in the selection of a suitable vacuum chamber metal, as certain metals used in the plasma chamber appear to have a marked effect on plasma focus formation [21].

The test gas was introduced into the plasma chamber using a Veeco PV-10 model precision leak valve. The fill gas pressure was monitored by a Hastings thermocouple gauge with a working range from .01 to 20 torr. This procedure was somewhat tedious but was adequate for our purposes.

4.4 Device Diagnostics

Instrumentation for the DPF experiment can be divided into two main areas, instrumentation associated with the electrical energy transferred to the pinch and instrumentation of the plasma focus properties, especially x-rays. The electrical measurements yielded information about energy transfer into the device in the form of breech current and voltage waveforms. During a satisfactory plasma focus the waveforms exhibited distinct features found only when a focus was formed. By viewing the current and voltage waveforms, the time from breakdown to pinch could be measured and in this way the gun could be tuned for a pinch during the current peak.

The primary plasma property of interest was x-ray emission from the focus, which was measured using solid-state detectors.

4.4.1 Electrical instrumentation

The basic design problems of the electrical instrumentation were fast response, adequate insulation against high-voltage breakdown from the large voltages developed at the breech, output signal levels less than 100 volts peak-to-peak, and sufficient shielding to provide reasonable signal-to-noise ratios. The designs which finally met these goals were a high-voltage capacitive divider and an air core Rogowski loop magnetic probe for current measurement. These designs were chosen because of simplicity and low cost construction as well as applicability and reliability. Several good references [27], [39]-[43] are available on high-voltage instrumentation that describe alternative methods with varying degrees of accuracy and applicability, but the methods chosen seemed the most appropriate.

The voltage divider and current probe were each connected by solid outer conductor coaxial cable to an individual plug-in unit of a dual beam model 555 Tektronix oscilloscope inside an electromagnetic interference screen room. By using the dual beam scope, a single photograph could be taken of the two waveforms simultaneously for a time comparison. The 555 also had delayed sweep capability, allowing sweep expansion for greater time resolution. Due to the peak voltage limitations of the plug-ins, the input signals had to be restricted to amplitudes less than 100 volts peak-to-peak. In environments with extremely high noise, probe signals are connected directly to the plates of CRT's for maximum speed and increased signal-to-noise ratios [43]. In our experiment, the noise levels were severe, but not to the point of requiring direct coupling of the instrumentation signals to the CRT deflection plates.

4.4.1.1 Voltage measurement device. The signal to be measured by the voltage measurement device is shown in Fig. 3b. The waveform rises very rapidly during the plasma focus to a level much greater than the applied bank voltage due to the sudden $\frac{dL}{dt}$ change when the focus forms. This voltage spike is of primary importance, thus dictating minimum requirements for the measurement device of a few tens of nanoseconds risetime response and the ability to withstand voltages several times the applied voltage, which in our case ranged from under 10 kV to 20 kV. The capacitive voltage divider was ideal for this application, with fast response, high-divider ratios with relatively small size, simple and inexpensive construction, and high-voltage capability. Other types of dividers such as resistive, compensated RC, or transmission-line reflection-type attenuators were built and tested, and found lacking either in linearity, noise rejection or cost effectiveness.

The capacitive divider design is shown in Fig. 16a. The capacitance of a coaxial cylinder capacitor is $C = 2\pi\epsilon_0\epsilon_1\ln\left(\frac{r_2}{r_1}\right)$ Farads where ϵ_1 = dielectric constant of the insulator, r_1 is the radius of the inside cylinder, r_2 is the radius of the outer cylinder, and d is the length of the cylinders in meters. With a third coaxial cylinder of radius $r_3 > r_2$, series coaxial capacitors are formed from the inner to the middle cylinder and from the middle to the outer cylinder. The ratio of the two capacitors is $C_1/C_2 = \epsilon_1\ln\left(\frac{r_3}{r_2}\right)d_1/\epsilon_2\ln\left(\frac{r_2}{r_3}\right)d_2$ where C_1 = inner capacitor and C_2 = outer capacitor. By applying the high-voltage signal to the inner cylinder with the outer cylinder referenced to ground, the voltage formed at the middle electrode will be equal to the signal voltage multiplied by the capacitive voltage divider ratio. This relationship is $V_0 = \frac{C_1}{C_1 + C_2} V_i$. Thus by making C_2 large and C_1 small, the desired divider ratio can be achieved. Fortunately, making C_1 small means making the annular spacing

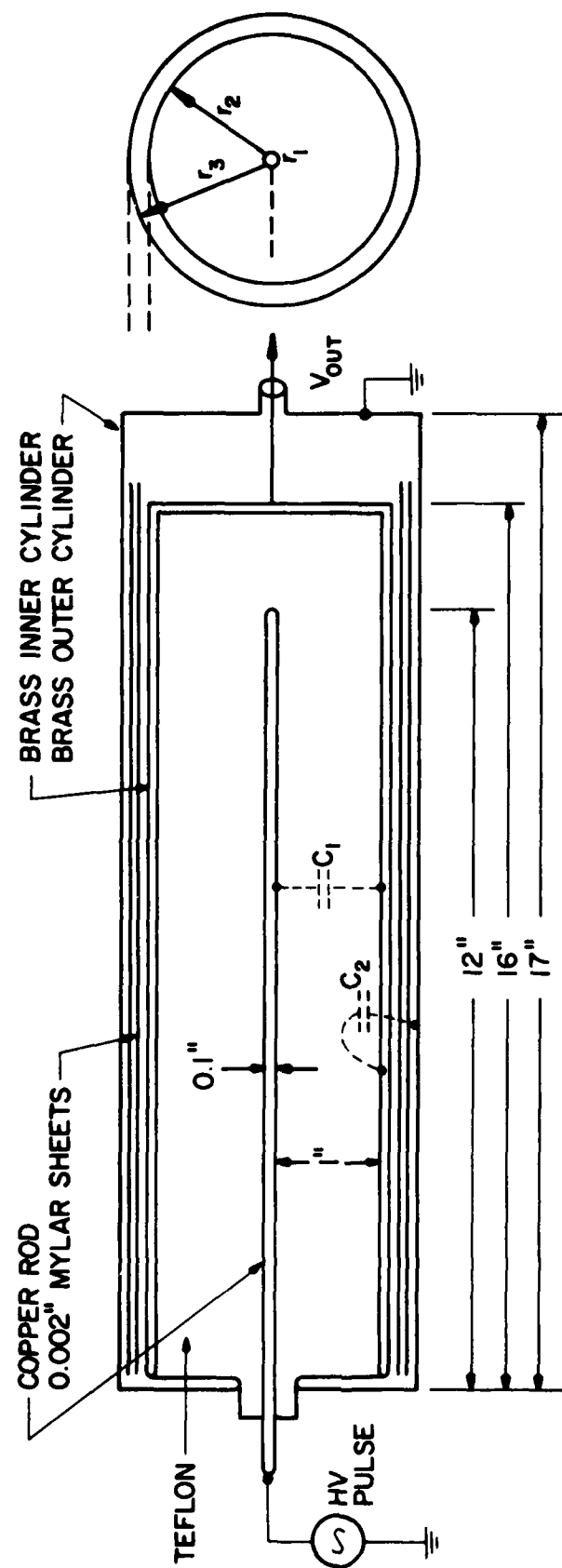


Fig. 16a. Coaxial capacitative high-voltage divider.

large which is desirable because the bulk of the high-voltage drop will be across C_1 and a large spacing is required to minimize breakdown of the intercylinder dielectric. C_2 will normally be about 1000 times smaller than C_1 , resulting in a spacing 1000 times smaller, but the voltage across this space will only be .001 times the signal voltage and will not overstress the thin dielectric of C_2 .

The coaxial geometry of the device offers excellent noise isolation because the outer cylinder acts as a noise shield as well as the voltage reference for the capacitive divider. Another advantage of this geometry is the convenient connection to coaxial cable afforded by the coaxial arrangement of the capacitors. Capacitive dividers also offer the advantage of simple adjustments of the divider ratios by adding the appropriate capacitance across the output of the device, effectively increasing C_2 and changing the divider ratio. The upper frequency response of the capacitive divider is limited by the inductance of the device [43] caused by the physical length of the cylinders. This defines a traveling wave condition which for our device results in a risetime of less than 10 nsec, well within acceptable limits. The low-frequency response is limited by the decay rate of C_2 with the input impedance of the scope. This was estimated by calculating the RC time constant of the divider and the scope, then choosing a 1 percent droop in the signal as the maximum allowable error. Such a calculation gives a cutoff frequency of 9 kHz, much lower than the lower frequencies of the signal since the experiments last only a few microseconds.

The divider is not matched to the coaxial signal cable until a resistor is inserted between the output capacitor and the coaxial cable. This resistor is chosen to match the characteristic impedance of the cable and, when properly chosen, will terminate all reflections that are reflected back to the divider. This resistor connection is shown in Fig. 16b. The

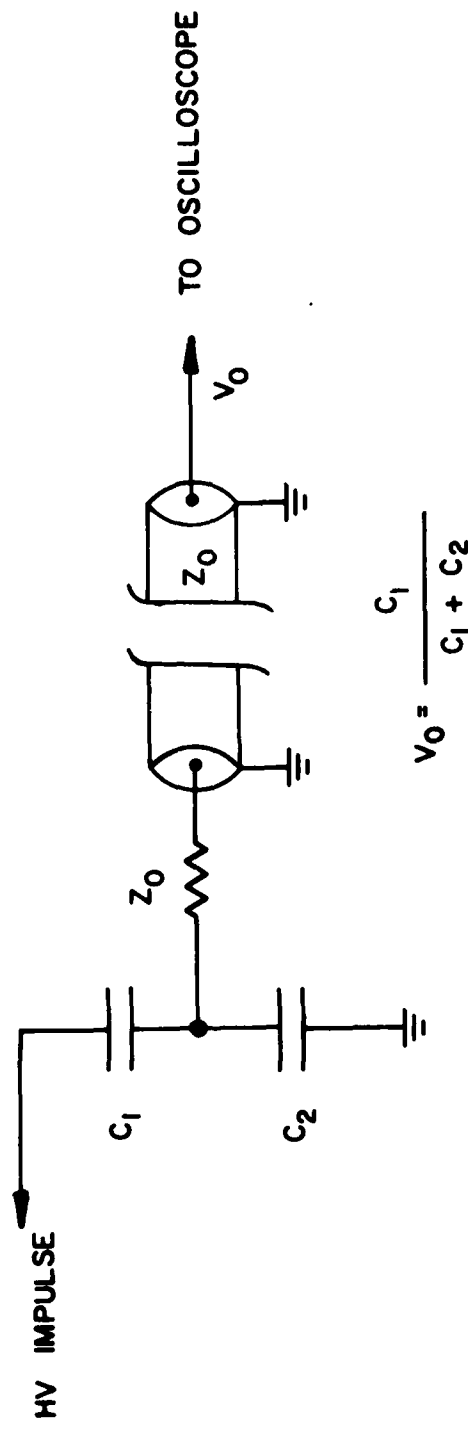


Fig. 16b. Capacitative divider circuit.

coaxial cable capacitance will also contribute an error in the signal if the cable capacitance is a sizeable portion of C_2 [42]. For our system, the coaxial cable had a lumped capacitance of 55 pF/m; thus with the 10 meter lines used in the experiment, the cable capacitance was about 550 pF. The value of C_2 used in the experiments was chosen to be 12,000 pF so the cable capacitance was not an appreciable amount.

The dimensions shown in Fig. 16a resulted in a value of C_1 of about 15 pF and C_2 of about 6000 pF. The resulting divider ratio was too small and had to be augmented by the addition of an additional 6000 pF capacitor connected across the output of the divider giving a final divider ratio of 800:1. A 51-ohm resistor was chosen for Z_0 to match the cable impedance.

The divider was fast, accurate, and able to measure voltages over 40 kV by virtue of the teflon insulator used between the inner and center cylinders. Teflon has a high resistance to surface tracking and allowed the outer cylinder shield to fit closely to the high-voltage inner cylinder without fear of flashover.

4.4.1.2 Current measurement device. Several alternatives for current measurement were considered. Among the most promising were current shunt, current transformer, magnetic probe and magneto-optic methods. The magneto-optic method was considered too costly and the current transformer method was found lacking in accuracy and response. Carefully designed current shunts, however, offer excellent response and high accuracy as well as simple calibration. The disadvantages of using current shunts are energy dissipation in the shunt resistance and the lack of electrical isolation since the shunt must be inserted directly into the circuit, making high-voltage differential measurements necessary. The Rogowski coil current probe offered reasonable accuracy, fast response as well as noncontact

current sensing, mobility, simplicity and low cost. In the end the choice was obvious, the Rogowski coil was acceptable in all the areas that the current shunt performed well but did not have the disadvantages of the current shunt.

A Rogowski coil, shown in Fig. 17a, is essentially a thin solenoid with N turns each with a cross-section area A that is bent into a closed loop of length S making an aperture through which a current can pass. The magnetic flux changes created by the current flowing through the aperture also pass through the center of the solenoid windings inducing a voltage in the coil windings which is related to the current I_0 flowing through the aperture. This relationship is given by $\int V dt = 4\pi \times 10^{-7} (NA/S) I_0$. The coil voltage must be integrated to produce a signal which is proportional to the aperture current. The integration can be accomplished quite simply by using an RC integrator connected to the coil output. In practical Rogowski coils one end of the coil is brought back through the interior of the windings to the other end of the coil [44]. In this way stray flux coupling error from the aperture formed by the coil output connection to the integrator is almost totally eliminated.

The RC integrator is normally constructed from carbon or metal-film resistors (not the spiral type) and the capacitor is usually a low-loss type such as silver mica for improved frequency response. The voltage developed across the capacitor is proportional to $\frac{1}{RC} \int V dt$. Thus it would seem that to maximize the signal output of the integrator, the RC time constant of the integrator should be as small as possible, but this is restricted by the low frequency response of the integrator. A common rule of thumb is to make the RC time constant at least 10 times as long as the longest period to be measured, which in our case was conservatively

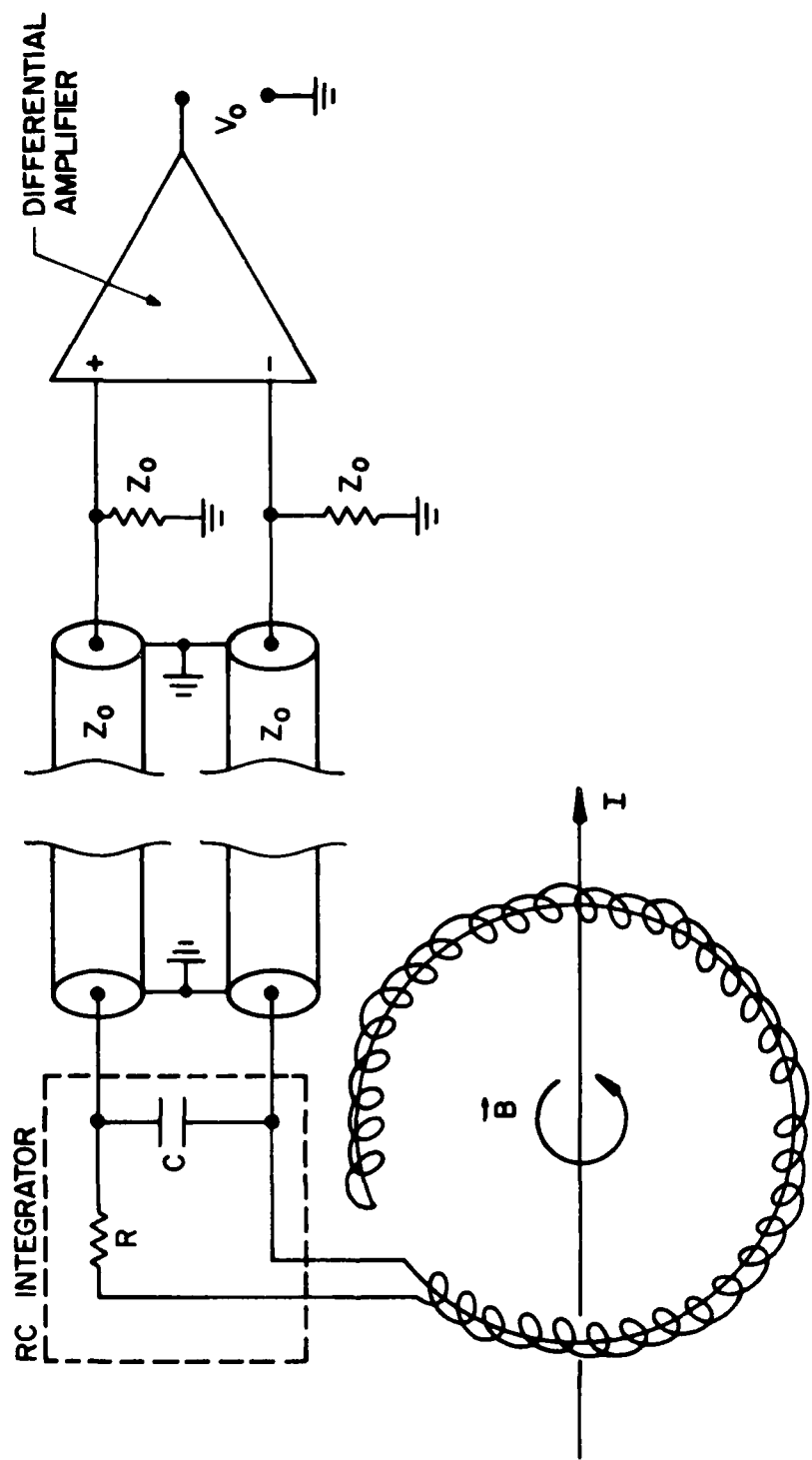


Fig. 17a. Rogowski loop circuit.

estimated to be 10^{-4} sec. Another integrator restriction is that the reactance ωL of the coil at the upper frequency of interest should be at least 10 times smaller than the resistance of the integrator. The greater the inductance of the coil, the more sensitive the coil is; therefore, the design of the Rogowski coil and integrator is a compromise between frequency response limits and sensitivity. Fortunately, in our case the currents were of such magnitude that sensitivity was not a major concern and frequency response could be increased.

For increased noise rejection, the Rogowski coil was measured using a differential technique by connecting each end of the integrator output to one side of a differential measurement system through solid outer conductor coaxial cables. A coil shield was connected to the shields of the coaxial cable and any noise induced in the shields was rejected by the common mode rejection ratio (CMRR) of the differential amplifier. The choice of a suitable differential amplifier was somewhat complicated by the high-frequency characteristics of the DPF-induced noise. The noise frequencies were mostly above 1 MHz and ordinary differential amplifier common mode rejection ratios fall off severely above 1 MHz. A simple yet satisfactory solution to this problem was to use a dual-trace scope plug-in unit in a subtraction mode. This method of differential signal extraction was preferential to the use of a dedicated differential amplifier plug-in unit because the dual-trace common mode rejection ratio did not fall off until 50 MHz.

The current probe design used in the experiments is shown in Fig. 17b. The shape of the winding core was such that the ground plane of the parallel plane transmission line feeder could pass through the aperture allowing maximum coupling to the probe. The probe was positioned near the transmission line connection to the outer electrode end plate because this point

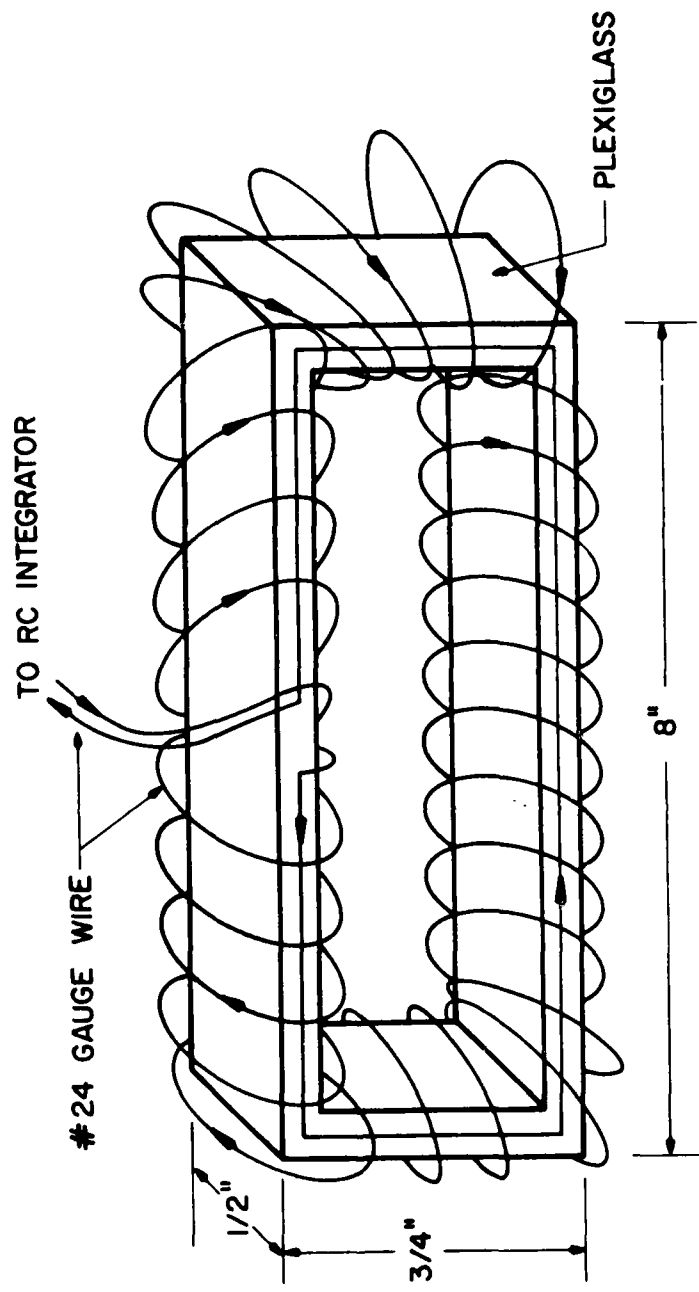


Fig. 17b. Rogowski loop current probe.

was easily accessible and also the voltage of the return plate with respect to the coaxial shields was due to the resistive drop along the transmission line from the end plate to the capacitor bank, which was relatively small. The coil was formed by 34 turns of #24 gauge wire with windings spaced as evenly as possible. The coil was then covered by copper braid which formed an electrostatic screen to decouple the coil from the high electric fields around the breech. Braid was used because the shield needed to be perforated to allow the magnetic flux through. The braid was connected to the coaxial cable shields and then carefully covered by many layers of teflon tape to insulate the braid from the high voltages in the breech area.

To insure that the detected signal was valid and not due to capacitively coupled noise, the probe was reversed such that the current direction into the coil aperture was reversed, and then the experiment was run again and the waveforms before and after the probe reversal were compared. The waveforms proved to be reversals of the other, indicating that the signal was indeed due to the current flow through the aperture of the coil. If the signals had been identical, then the waveforms would have been due to capacitively coupled signals.

4.4.2 X-ray measurements

The plasma property of primary interest in our experiment is the x-ray pulse produced during the plasma focus. During early stages of development optical photographs of the pinch were taken using an ND-16 neutral density filter added to reduce the light intensity to an acceptable level. These photographs yielded information about the pinch symmetry and reproducibility of the pinch. In addition to optical photographs, solid-state detectors were used.

Double-diffused PIN silicon detectors were used to obtain time-resolved information of pinch performance. The detectors, model number 100-PIN-125, were purchased from Solid State Radiations Corporation. The detector circuitry is shown in Fig. 18. The diode collector area is 100 square millimeters with a sensitive depth of 125 μm at an operating voltage of 200 V. These detectors are well-suited for use with pulsed plasma devices because of their inherently fast risetime and high detection sensitivity. The risetime of these detectors is related to their thickness divided by the bias voltage and is less than 5 nsec for the devices used in this experiment. Silicon PIN detectors are capable of producing signals proportional to incident x-ray intensity and can be used for quantitative x-ray spectra measurements by employing the Ross filter technique [47].

The silicon detectors were extremely useful when tuning the plasma gun for plasma focus at current peak. Simultaneously triggering the oscilloscopes that recorded the current, voltage and x-ray waveforms allowed a time comparison of the x-ray pulse, current dip and voltage spike associated with plasma focus. The x-ray waveforms were extremely noise-free, as signal levels recorded during nonpinch experiments were less than 10 mV as compared to signals greater than 30 V recorded during strong pinches. The x-ray waveforms indicated x-ray pulses during pinch ranging from less than 100 nsec up to several hundred nsec, often with several distinct x-ray bursts during a single pinch.

4.5 Shielding and Grounding

With the high currents and short times associated with capacitive storage systems, $\frac{di}{dt}$'s reach 10^{12} A/sec producing stray voltages due to nanohenry stray inductance on the order of tens of volts. Megamp currents produce kilovolts across the milliohm resistance found in

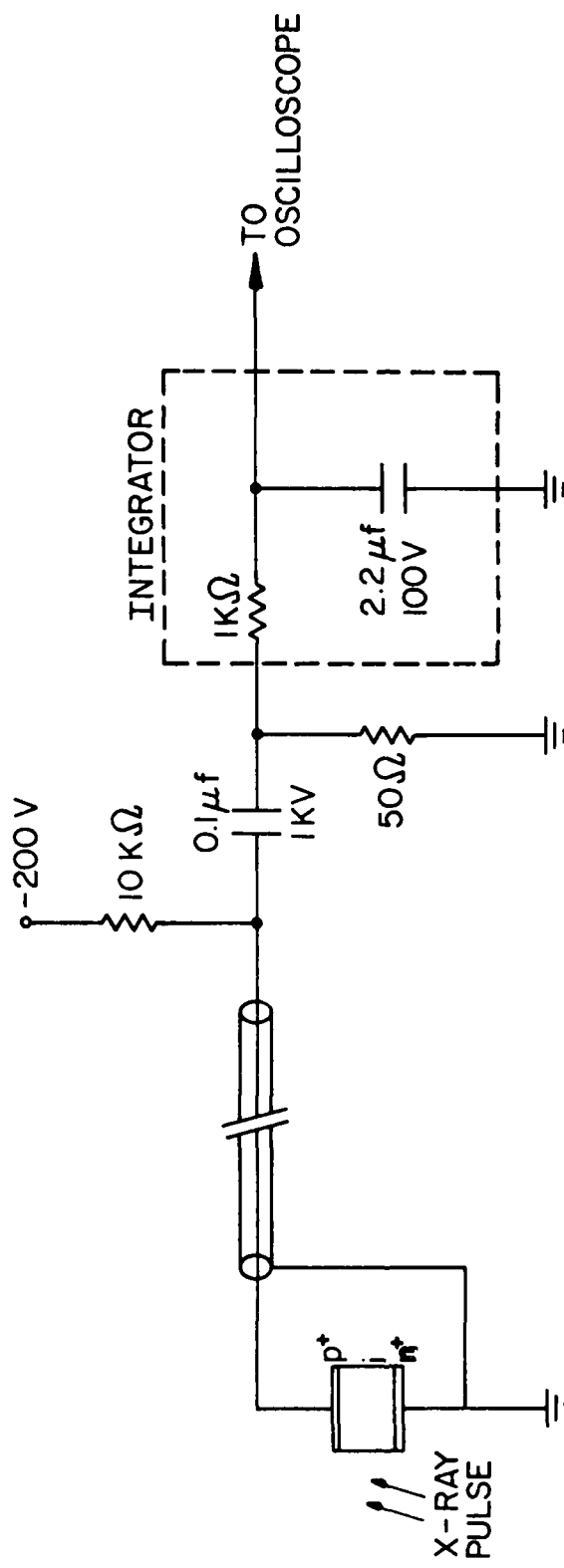


Fig. 18. Solid-state x-ray detector circuit.

ordinary hook-up wire. Such large uncommon voltages illustrate the shielding and grounding problems encountered in dense plasma focus research.

For safety, it is important that all ground leads be as large in size and as low in resistance as possible. Grounding to the "water pipes" should be avoided as megamp ground currents can produce lethal voltages. Also, ground loops in instrumentation and charging systems are to be avoided for previously mentioned safety reasons and because large current flow in instrumentation grounds may cause large common mode signals as well as severe transient coupling to the signal. By practicing the single-point ground method of system grounding, our system was assured of greatly reducing destructive and lethal ground loops. Ground straps were made from two-inch copper braid and, where distances were large, two straps were connected in parallel. The dense plasma focus system, the storage bank, and the charging system were all placed on top of, and connected to, a large copper sheet forming a ground plane which was in turn connected via two large ground straps to a 6' long, 1" diameter copper rod driven into the earth outside the lab area. The instrumentation screen room was also connected to the ground plane via two large ground straps.

Due to the large electromagnetic fields produced during device operation, measurement noise became a severe problem when initial measurements using ordinary shielding techniques allowed noise levels of tens of volts into diagnostic signals. Even after doubly shielding braided coaxial cable with an extra braid shield, the noise levels were not greatly reduced. It was evident more rigorous shielding practices were necessary.

A brief search of electromagnetic interference (EMI) literature, especially the IEEE Transactions and Electromagnetic Compatibility, revealed an almost overwhelming amount of literature on the subject, but it was apparent that solid outer conductor coaxial cable and a screen room were definitely required.

The solid outer conductor coaxial cable finally selected was a 51-ohm, foam dielectric armored Heliax cable produced by the Andrew Company. Standard electrical connections for the Heliax cable were not compatible with the N-type connections used in our system, and special hybrid connectors were constructed to maintain the shielding integrity of the coaxial cable as well as to mate with existing N-type fittings. Great care was required when installing these hybrid connectors because the connectors were soldered to the coaxial shield and the foam dielectric often melted when heated to soldering temperatures. The cables with connectors were tested up to 2 kV without breakdown and would pass nanosecond risetime pulses without noticeable degradation.

The screen room was constructed from 1/16" thick copper sheets, overlapped and soldered where possible. Where soldering was prohibited, copper tape was used to seal all gaps. Copper sheet 1/16" thick provides greater than 160 dB attenuation of EMI [45] at frequencies near 1 MHz, which is the time scale of the experiment. The door was made "noise-tight" by fastening copper flaps around the outside edge of the door which pressed firmly against the copper walls of the screen room. Lighting was necessarily incandescent as fluorescent lighting produced RF noise. A battery-operated AM/FM radio was used to test the effectiveness of the shielding by tuning to strong local stations and listening for a reduction in reception.

One important factor overlooked initially was filtering of the ac power into the screen room. When unfiltered power was introduced into the screen room, radio signals were received as strongly as if no screen room existed. Model 10R3, 10 A, 115 V ac power filters were purchased from the Corcom Company and installed with immediate success. The ac power control lines to the HV charging system relays were also filtered.

All bulkhead feedthroughs were soldered in place to maintain shielding integrity, and all unused coaxial cables were capped during testing.

Another shielding problem more readily solved was the problem of x-ray shielding the dense plasma focus. Lead shielding 1/8" thick was attached to plywood panels which fastened to the supporting framework of the device. The lead protruded about 3" around the edges of the plywood panels allowing the lead to be folded over at the corners to provide effective x-ray shielding. Doors were made in the enclosure to permit access to device diagnostics and the vacuum chamber.

4.6 High-Voltage Charging System

High-voltage capacitor lifetimes are greatly reduced when operated for long periods at rated voltages. Therefore, capacitor banks should be charged in as short a time as possible. Saturable reactor circuits and constant $\frac{dv}{dt}$ charging are often used to achieve rapid charging rates. Our system operated with a much simpler yet relatively effective method of charging at high currents by applying a voltage much larger than the desired voltage to the charging resistor network, then sensing when the bank voltage had reached a selected voltage, at which time the charging voltage was removed from the bank. In this way the charging current remained high, being limited by the series charging resistance chosen so that the current maximum would not exceed the current ratings of the power supply.

The high-voltage charging system is diagrammed in Fig. 19 and the voltage control and sensing electronics are shown in Fig. 20. The high-voltage control system senses the capacitor bank voltage attenuated by a divide-by-1000 voltage divider, and the control system compared this voltage to a precision variable voltage source. When this voltage reference is attained by the bank, a Schmidt trigger causes the control relay R1 to drop out, which removes ac power from the high-voltage relays causing them to open, thus removing the high-voltage power supplies from the charging circuits. The variable precision voltage reference allows selection of bank voltages from a few hundred volts to 19 kV. In this way consistent and repeatable bank voltages were easily attained.

The control system was designed to provide a measure of safety as well. The control system requires not only ac power to the screen room, but also a manual arming command before the bank can be charged, thus requiring some degree of forethought before application of high voltage. More sophisticated systems often include screen room door interlocks, fill gas pressure interlocks and various instrumentation interlocks that are required conditions that must be met before the device can be fired.

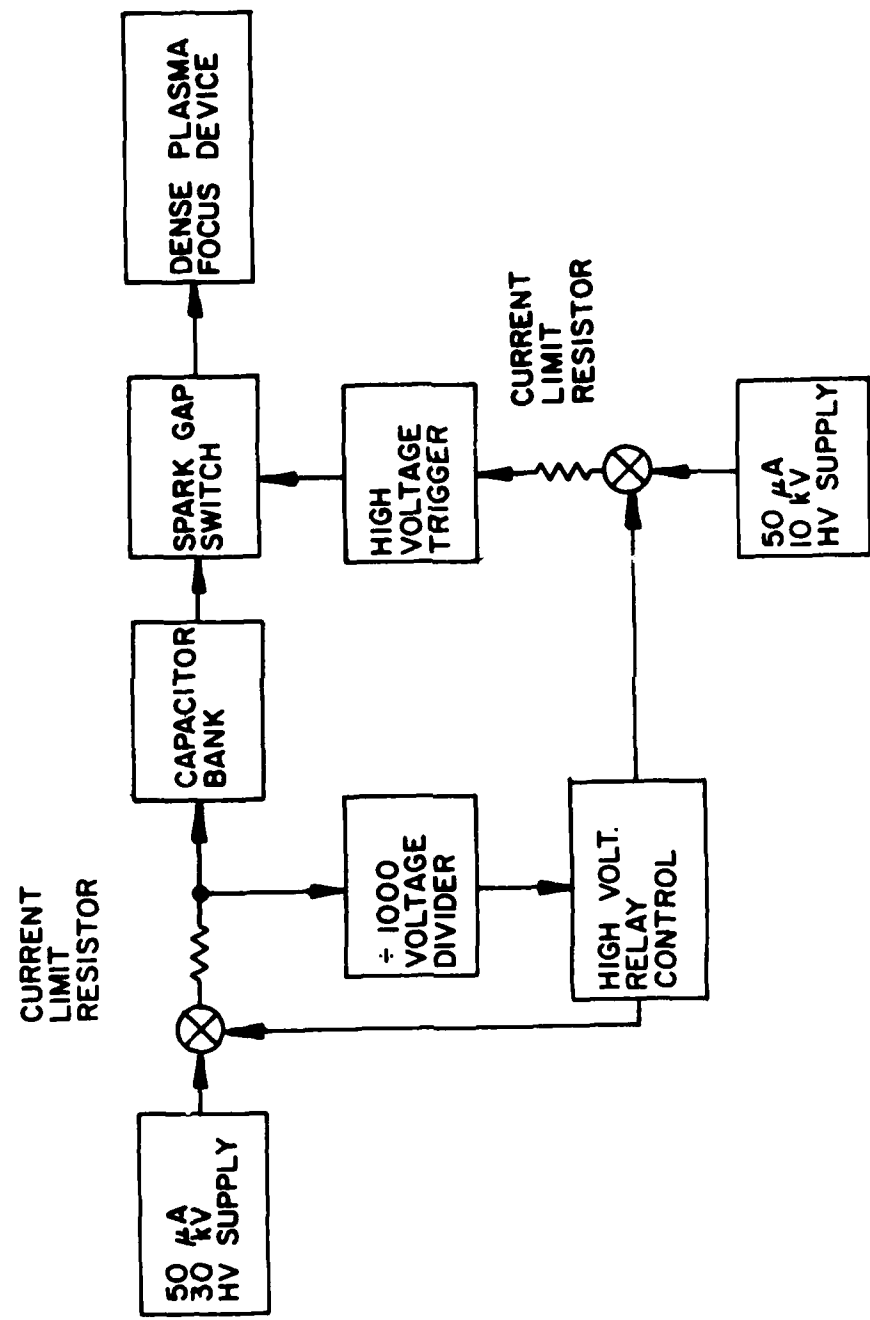


Fig. 19. High-voltage system.

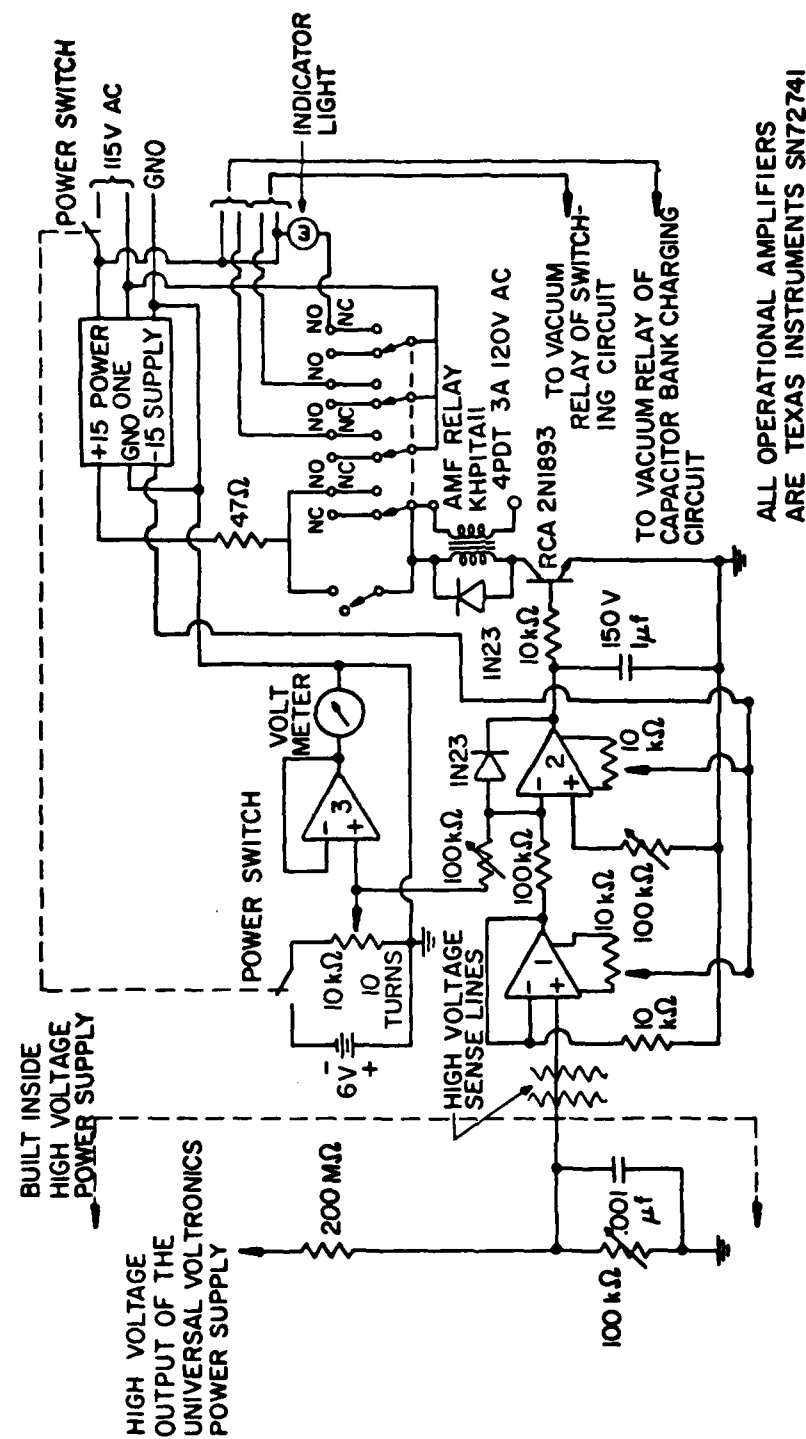


Fig. 20. High-voltage control sensing circuit.

5. DEVICE OPERATION

The dense plasma device operation was deemed satisfactory after meeting three requirements: consistent performance, x-ray production and reliable operation. The device performed consistently after moderate conditioning of the electrode insulator. Conditioning was required after every cleaning of the insulator and especially when a newly constructed insulator was used for the first time. Conditioning consisted of repeated firing of the device (up to 15 shots) with bank voltages ranging from 14 to 15 kV at 1 torr pressure. It is not known whether higher or lower voltages affect the conditioning rate. Proof of sufficient conditioning was determined by the appearance of sizeable voltage pulses (greater than .5 V) from the solid-state x-ray detector. Once conditioning was achieved, the x-ray detector waveform remained very consistent for shots with the same bank voltage and test gas pressure.

The x-ray detector waveforms appeared to be a reliable indicator of x-rays, but the data are totally uncalibrated. Because of the detector signal repeatability for a given voltage and pressure and the absence of electromagnetic interreference coupling into the x-ray detectors, it is reasonable to assume that the detector waveforms were dependable indicators of x-ray production.

The device was also made relatively reliable but only after considerable development. Elkonite inserts in the plasma gun center electrode tip and the spark gap electrodes provided very effective retardation of arc erosion of these surfaces. After several hundred spark gap shots, the gap electrode showed only a slight circular depression about 1/16" deep in the center of the Elkonite. The plasma gun center electrode tip showed a smoothing of the edges of the tip with a striated etch pattern radiating

from the center of the Elkonite insert. The etching depth was less than 1/16" deep.

The Pyrex cross vacuum chamber showed substantial pitting and darkening, apparently from electrode material sputtering onto the glass. This coating did not impair device operation. It only became an inconvenience as visual observations of the device became more difficult.

At one time during testing, the Rogowski coil current probe was destroyed when the teflon insulator covering the electrostatic shield broke down. In another instance, breakdown occurred between the upper and lower housings of the spark gap. The problem of high-voltage breakdown was always present and, after substantial repair of the capacitor bank voltage monitor circuitry damaged by the breakdown of the transmission line insulator, the overall system was upgraded for increased high-voltage standoff capability by increasing insulator thickness wherever possible and rounding all sharp metal edges. The system did not incur any further breakdown after this upgrade and has performed reliably ever since.

The device was operated with a variety of bank voltages and test gas pressures. The voltages were varied from 9 kV to 19 kV with a variety of gas pressures. The device did not produce appreciable x-rays until the bank voltage was raised to 13 kV, no matter what the gas pressure. The gas pressure was varied from .5 torr to 5 torr, but x-ray pulses were very weak below .75 torr and above 1.5 torr with an optimum pressure about 1 torr. The time from breech breakdown to pinch formation could be varied slightly by changing the applied voltage and gas pressure. The change in sheath arrival time followed qualitatively the predictions of the sheath snowplow theory discussed in Section 2.2, but quantitative measurements were not made. Only a few hundred nanosecond change in arrival time is all that could be made.

6. SUMMARY

The dense plasma focus device system discussed in this paper is a qualified success. Although optimization of bank parameters to match device characteristics was not realized, relatively satisfactory operation has been achieved and x-ray production during pinch verified. At present, quantitative measurement of x-ray production during pinch has not been implemented, and, while desirable, is not necessary to show fundamental device operation, and is rather inconsequential when compared to the successful development of techniques and devices needed to produce a working DPF system.

Some of the more significant accomplishments are: the development of a shatter-resistant electrode insulator; a mechanical-shock-resistant breech design; a high-current, relatively low-inductance air dielectric spark gap and gap trigger system; an automatic capacitor bank charging system for repeatability; an electromagnetic interference isolated screen room; a fast-risetime, high-current probe; and a fast-risetime, high-voltage probe.

REFERENCES

1. J. G. Linhart, Nucl. Fus. 10, 211 (1970).
2. J. W. Mather, Phys. Fluids Suppl. 7, 5-28 (1964).
3. J. W. Mather, Phys. Fluids 8, 366 (1965).
4. P. P. Petrov, N. V. Filippov, T. I. Filippova, and V. A. Khrabrov, Plasma Physics and the Problems of Controlled Thermonuclear Reactions, M. A. Leontovich, ed. (Pergamon, New York, 1960), Vol. 4, p. 198.
5. N. V. Filippov, T. I. Filippova, and V. P. Vinogradov, Nucl. Fus. Suppl. Pt. 2, 577 (1962).
6. J. W. Mather, Methods of Experimental Physics, R. H. Lovberg and H. R. Griems, eds. (Academic Press, New York, 1971), Vol. 9b, p. 187.
7. J. W. Mather and A. H. Williams, Phys. Fluids Res. Note 9, 2081 (1966).
8. M. Rosenbluth and R. Garwin, Los Alamos Sci. Lab. Rep. LA-1850. Los Alamos Sci. Lab., Los Alamos, New Mexico (1954).
9. J. W. Mather and P. J. Bottoms, Phys. Fluids 11, 611 (1968).
10. M. J. Bernstein, D. A. Meskan, and H. L. L. van Paassen, Phys. Fluids 12, 2193 (1969).
11. H. L. L. van Paassen, R. H. Vandre, and R. S. White, Phys. Fluids 13, 2606 (1970).
12. M. J. Bernstein, Phys. Rev. Letters 24, 724 (1970).
13. N. W. Jalufka and J. H. Lee, Phys. Fluids 15, 1954 (1972).
14. P. J. Bottoms, J. P. Carpenter, J. W. Mather, K. D. Ware, and A. H. Williams, Plasma Physics and Controlled Nuclear Fusion Research (1968), Vol. 2, p. 67.
15. N. J. Peacock, M. J. Forest, M. G. Hobly, and P. D. Morgan, 5th European Conf. Cont. Fus. and Plasma Phys. (1972), Vol. 1, p. 66.
16. M. J. Bernstein, Phys. Fluids 13, 2858 (1970).
17. M. J. Bernstein and G. G. Comisar, Phys. Fluids 15, 700 (1972).
18. S. P. Gary and F. Hohl, Phys. Fluids 16, 997 (1973).
19. D. E. Potter, Phys. Fluids 14, 1911 (1971).
20. M. H. Dazey, H. L. L. van Paassen, and V. Josephson, J. Appl. Phys. 41, 3545 (1970).
21. D. W. Kerst, Rev. Sci. Instr. 36, 1670 (1965).

22. J. W. Mather, P. J. Bottoms, J. P. Carpenter, A. H. Williams, and K. D. Ware, *Phys. Fluids* 12, 2343 (1969).
23. R. S. Post and T. C. Marshall, *Phys. Fluids* 17, 452 (1974).
24. R. L. Gullickson, Lawrence Livermore Laboratory Report UCID-16892. Lawrence Livermore Laboratory, Livermore, California (1975).
25. R. A. Gross and B. Miller, Methods of Experimental Physics, R. H. Lovberg and H. R. Griems, eds. (Academic Press, New York, 1970), Vol. 9a, p. 169.
26. W. C. Nunnally, M. Kristiansen, and M. O. Hagler, *IEEE Trans. Instrum. Meas.* 24, 112 (1975).
27. F. B. A. Frungel, High Speed Pulse Technology (Academic Press, New York, 1965), Vol. 1, p. 59-171.
28. A. S. Denholm et al., "Review of Dielectrics and Switching," Air Force Weapons Lab Technical Report AFWL-TR-72-88, p. 417-503 (1972).
29. J. M. Lafferty, *Proc. IEEE* 54, 23-32 (1966).
30. G. N. Aretov, V. I. Vasil'ev, M. I. Pergament, and S. S. Tserevitinov, *Sov. Phys.—Tech. Phys.* 11, 1548-1555 (1967).
31. W. C. Nunnally, Ph.D. Thesis, Texas Tech. University, Lubbock, Texas (1974).
32. J. E. Gruber, *Rev. Sci. Instr.* 39, 1740 (1968).
33. P. M. Barnes, J. E. Gruber, and T. E. James, *J. Sci. Instr.* 44, 599 (1967).
34. J. E. Gruber and T. E. James, *Proc. IEE* 115, 1530-1534 (1968).
35. T. E. Broadbent and A. H. A. Shlash, *Proc. IEE* 112, 2152-2158 (1965).
36. P. I. Shkuropat, *Sov. Phys.—Tech. Phys.* 11, 779-783 (1966).
37. P. I. Shkuropat, *Sov. Phys.—Tech. Phys.* 14, 943-948 (1970).
38. G. A. Mesyats, Y. I. Bychkov, and A. I. Iskol'dskii, *Sov. Phys.—Tech. Phys.* 13, 1051-1055 (1969).
39. E. Kuffel and M. Abdullah, High Voltage Engineering (Pergamon Press, Oxford, 1970).
40. G. W. Bowder, Measurements in High Voltage Test Circuits (Pergamon Press, Oxford, 1973).
41. A. J. Schwab, High Voltage Measurement Techniques (MIT Press, Cambridge, 1972).

42. J. D. Craggs and J. M. Meek, High Voltage Laboratory Technique (Buttersworth Publications Ltd., London, 1954).
43. R. J. Thomas, IEEE Trans. Instrum. Meas. IM-19, 102 (1970).
44. R. H. Huddlestone and S. L. Leonard, Plasma Diagnostic Techniques (Academic Press, New York, 1965).
45. J. Severinsen, "Designer's Guide to EMI Shielding, Part 1," Electronic Design News 19, 47 (1975).
46. D. J. Johnson, Rev. Sci. Instr. 45, 191-194 (1974).